Effects of surface tension on a floating body in two dimensions

Fei Zhang[1], Xinping Zhou[1,2],† and Chengwei Zhu[1]

[1]Department of Mechanics, Huazhong University of Science and Technology, Wuhan 430074, PR China

[2]Hubei Key Laboratory for Engineering Structural Analysis and Safety Assessment, Wuhan 430074, PR China

A model for calculating the force profile and the moment profile of a floating body in two dimensions with an arbitrary cross-section is proposed. Three types of cross-sections with different contact angles and densities are calculated by using the model to determine the vertical and rotational equilibria and their stabilities. Results show that the model can be applied to convex floating bodies with finitely many sharp edges. The study is then extended to investigate the surface tension effects on the vertical and rotational stabilities by varying the following parameters: the radii of curvature of the solid surface at the contact lines and the size of floating body. In general, the smaller the radii of curvature the better the vertical and rotational stabilities. However, for the contact angle $\theta = 0$ (or $\theta = \pi$) the radii of curvature have no effect on the vertical stability of the floating body. By varying the size of the floating body, it is found that the vertical and rotational stabilities of mesoscale floating bodies vary continuously between the stabilities of the macroscale and microscale floating bodies with other parameters remaining unchanged.

Key words: capillary flows, mathematical foundations, variational methods

---

1. Introduction

An understanding of the hydrostatics of floating bodies is important in a number of practical applications, including the design and optimization of ships (Biran 2003), the capillary-driven self-assembly of mesoscale components (Bowden *et al.* 1997) and the stabilization of emulsions by colloidal particles (Tavacoli *et al.* 2012). In these examples, the importance of gravitational forces compared to surface tension forces, measured by the Bond number (Bo), varies qualitatively. In contrast to macroscale floating bodies ($Bo \gg 1$), surface tension plays an important role in floating bodies (mesoscale or microscale) with $Bo \sim 1$ or $Bo \to 0$, which may give rise to a disturbed water surface. The meniscus will add more complexities and new properties to the floating phenomena, which may lead to unexpected behaviours, such as the floatation of relatively dense bodies and multiple equilibrium floating positions (see Vella (2015) for a review).

† Email address for correspondence: xpzhou08@hust.edu.cn

To understand the floating phenomena, it is necessary to deal with the conditions of equilibria of floating bodies. For macroscale floating bodies, the formulation of the vertical equilibrium of forces is provided by Archimedes' principle while the horizontal equilibria are not taken into account without the effects of surface tension; the equilibria of moments are determined by the relationship between the centres of gravity and buoyancy (Biran 2003). For floating bodies (mesoscale and microscale) under the effects of surface tension, the formulations of equilibria are given by the balance of forces acting on the bodies, including the buoyancy force, the weight force and the capillary force (Bhatnagar & Finn 2006; Vella, Lee & Kim 2006); the equilibria can also be determined by the minimization of free energy (Rapacchietta, Neumann & Omenyi 1977). Regardless of the position and shape of the contact line, the resultant moment on an isotropic particle with respect to its centre due to surface tension is always equal to zero (Singh & Hesla 2004).

Regarding the capillary floating problems, the calculations of the forces exerted on floating bodies require the shape of the deformed meniscus, which can be determined by solving the Young–Laplace equation with Young's relation as the boundary condition. However, the Young–Laplace equation can only be solved for the problems with axial symmetry (Concus 1968; Padday 1971; Majumdar & Michael 1976) or under the two-dimensional hypothesis (Bhatnagar & Finn 2016). In these cases, the Young–Laplace equation is expressed as an ordinary differential equation (ODE) retaining its nonlinearity. For the axisymmetric cases, the Young–Laplace equation can be solved numerically or by a perturbation method for its asymptotic solutions, e.g. a meniscus forming in the circular capillary (Concus 1968), a pendent drop suspended from a solid surface (Majumdar & Michael 1976) and a sessile drop resting on a solid surface (Padday 1971). For the two-dimensional cases, the analytic solutions of the Young–Laplace equation can be obtained by direct integration (Miersemann 2015) or integrating its parametric form (Princen 1969; Finn 2010; Aspley, He & McCuan 2015; Bhatnagar & Finn 2016); the solutions can be classified into two families of curves and four barrier curves according to the constant of integration (Bhatnagar & Finn 2016). The Young–Laplace equation can also be solved with a linearization assumption, valid when the inclination angles of the menisci are small. For multiple-particle configurations, a superposition approximation due to Nicolson (1949) is extensively applied for determining the interface around isotropic (Chan, Henry & White 1981; Oettel, Dominguez & Dietrich 2005) and anisotropic (Stamou, Duschl & Johannsmann 2000) particles, which may lead to a violation of boundary conditions at small distance between particles. In two-particle configurations, the bipolar coordinates can be introduced for transforming the linearized Young–Laplace equation, where boundary conditions are imposed correctly (Kralchevsky *et al.* 1992; Paunov *et al.* 1992).

In general, it is difficult to calculate the equilibrium configurations of small floating objects on a water surface. This calculation requires that the force balance equations of particles and the Young–Laplace equation for the surrounding menisci are solved simultaneously. This means that the menisci and the forces exerted on the particles affect each other. An alternative for determining the equilibrium configurations of the particles is to find the configurations (the stable equilibria) with minimum energy (Soligno, Dijkstra & Van Roij 2016). Numerical techniques employed for minimizing energy are, e.g. a gradient descent method (Brakke 1992), and a simulated annealing algorithm (Soligno, Dijkstra & Van Roij 2014). It is well known that the menisci minimizing energy are the stable equilibria while the solutions of the Young–Laplace equation are the equilibria (stable or unstable) of menisci. In contrast to the use

of theoretical methods to solve the Young–Laplace equation, numerical iteration techniques to evolve energy are applicable in most cases; however, the numerical iteration techniques cannot be used to obtain any formulae for explanations, which may lead to a concealment of some of the remarkable properties of floatation. For example, the variational formula for the floating bodies in an unbounded (Bhatnagar & Finn 2006) or bounded (Treinen 2016) fluid finds two possible equilibrium floating positions and predicts their stabilities by the variational method.

As already mentioned, a number of studies have dealt with the equilibrium configurations of floating bodies. Those studies can be divided into two groups according to the method of stability analysis, including the minimization of energy (Soligno *et al.* 2016) and the second variation of energy (Bhatnagar & Finn 2006). The first group finds the local energy minima by plotting the total free energy as a function of the orientation of the particle. The reason why the position of the particle is not considered can be explained by the fact that the position of the particle in general is unique for the configuration of minimal energy (if it exists) with a fixed particle orientation. By contrast, the second group calculates all of the equilibrium configurations by using the mechanical equilibrium conditions (derived from the first variation of energy) and then investigates their stabilities according to the second variation of energy. In all of these studies, there is more than one equilibrium configuration, where the unstable equilibria are neglected in the first group. For instance, there are at least four distinct equilibrium orientations satisfying Young's relation for a two-dimensional convex particle at a planar interface without gravity; half of them are stable, where the stabilities depend on the orientation, the geometry and the contact angle of the particle (Raphaël *et al.* 1992). For the case only affected by gravity, the stability of a floating body is determined by its orientation, geometry and distribution of mass, measured by the metacentric height (Biran 2003). It is noted that surface tension and gravity affect the stability of floating bodies in a different way. For example, a body in two dimensions only under the effects of surface tension cannot float in a stable equilibrium with the liquid interface intersecting the interior of a straight side at a single point (Kemp & Siegel 2011), while the restriction just described is inappropriate for macroscale floating bodies. To the best of our knowledge, the effects of both surface tension and gravity on the equilibria and their stabilities of a floating body with an arbitrary cross-section have not been studied previously.

In this paper, a mathematical model that considers the effects of gravity and surface tension is proposed to calculate the resultant force and moment of a floating body with an arbitrary cross-section and to determine their stabilities by the first derivatives of force and moment. The mathematical model is based on a force decomposition different from Keller (1998). Three types of cross-section are calculated by using the model to determine the vertical and rotational equilibria and their stabilities. Then the study is extended to investigate the surface tension effects on the vertical and rotational stabilities by varying the following parameters: the radii of curvature of the solid surface at the contact lines and the size of the floating body.

2. Model

Consider a long cylinder with an arbitrary convex cross-section floating horizontally on the surface of an unbound liquid in a downward gravity field, as depicted in figure 1. Physically, the equilibrium of the cylinder is supported by the pressure force $\boldsymbol{P}$ due to hydrostatic pressure p and the surface tension forces $\boldsymbol{f}_t^l$ and $\boldsymbol{f}_t^r$ at the
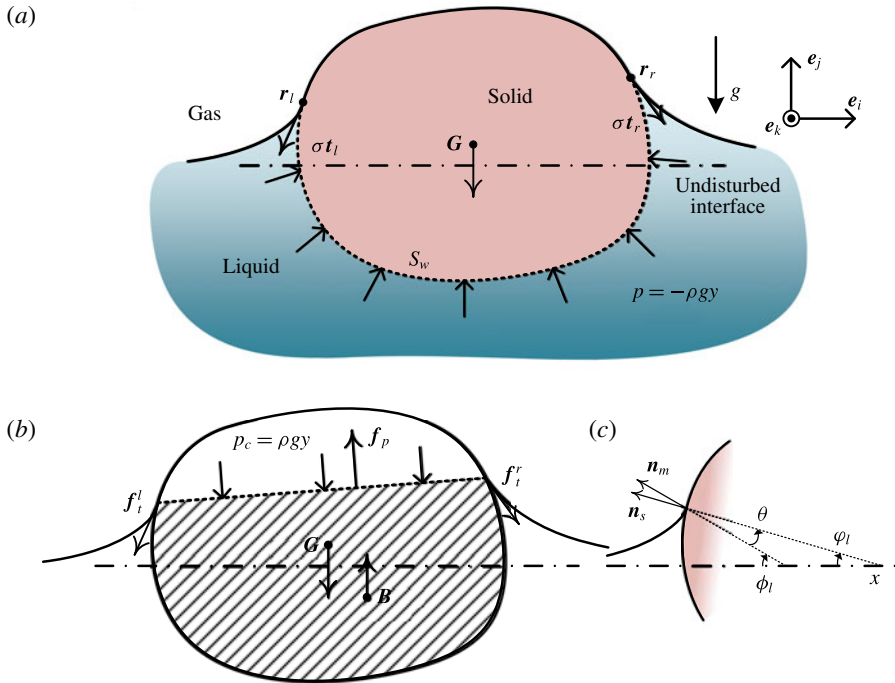
FIGURE 1. (Colour online) Schematics of a cylinder with an arbitrary cross-section lying on a surface: (*a*) the real force conditions, (*b*) the equivalent force conditions of the cylinder and (*c*) the geometric relations at the left contact point. The position vectors of the left and right contact points are denoted by $\boldsymbol{r}_l$ and $\boldsymbol{r}_r$, respectively. The line pressure p_c is exerted on the straight line L_c between the contact points. The orthonormal basis vectors $\boldsymbol{e}_i$, $\boldsymbol{e}_j$ and $\boldsymbol{e}_k$ define a Cartesian coordinate system. The origin can be any point on the undisturbed water line, where (x, y, z) are the Cartesian coordinates.

contact points (contact lines in three dimensions), as shown in figure 1(*a*). However, the pressure force $\boldsymbol{P}$ in general is difficult to calculate due to the geometry of the solid. By means of the Green formula, the integral over the wetted surface S_w of the solid is transformed to the buoyancy $\boldsymbol{B}$ (analogous to the buoyancy in Archimedes' principle) and the integral over the straight dashed line (see figure 1*b*), while the calculation of the pressure force $\boldsymbol{P}$ is different from that in previous studies (see Mansfield, Sepangi & Eastwood (1997), Keller (1998)). The application of the Green formula leads to a considerable simplification of the problem. A mathematical model for the conditions of equilibria and stabilities of the cylinder is presented, based on four forces, including the weight force $\boldsymbol{G}$, the surface tension forces $\boldsymbol{f}_t^l$ and $\boldsymbol{f}_t^r$, the buoyancy $\boldsymbol{B}$ and the compensating pressure force $\boldsymbol{f}_p$ due to line pressure p_c, see figure 1(*b*). The line pressure p_c is the fictitious pressure exerted on the straight line L_c between the contact points, which is deduced from the application of the Green formula on the pressure force $\boldsymbol{P}$.

The model derivation is based on the following assumptions.

(i) The cylinder is long enough for the three-dimensional end effect to be negligible, i.e. all quantities and calculations are two-dimensional.

(ii) The cylinder surface is ideally smooth and has a constant contact angle θ so that contact angle hysteresis is not considered. The cylinder can have finitely many sharp edges.

(iii) The cross-section is convex so that the meniscus (if it exists) can be uniquely determined by the contact angle and the position and orientation of the cylinder. The uniqueness argument is provided in appendix A.

2.1. *Geometric constraints*

In two dimensions, as the liquid surface is in equilibrium, the menisci at the two sides of the cylinder can be expressed as (Bhatnagar & Finn 2016)

$$\frac{\kappa u^2}{2} + \cos \psi = 1, \quad \psi \in [-\pi, \pi], \tag{2.1}$$

where u is the height of the meniscus, ψ is the inclination angle of the meniscus and $\kappa = \rho g / \sigma$ is the capillary constant, with the density difference ρ(positive) between gas and liquid, the gravitational acceleration g and the surface tension σ of the interface. Equation (2.1) can be obtained by integrating the parametric form of the Young–Laplace equation in two dimensions (which gives a conserved quantity $C = \kappa u^2/2 + \cos \psi$) and then determining $C = 1$ from the condition at infinity (Princen 1969; Finn 2010; Aspley *et al.* 2015). Since the sign of the height u is the same as that of the inclination angle ψ, the expression of the height u can be given by transforming (2.1)

$$u = \frac{2}{\sqrt{\kappa}} \sin \frac{\psi}{2}. \tag{2.2}$$

To omit unnecessary details, only the left side of the cylinder is considered, as shown in figure 1(*c*). The origin is arbitrary on the water line because the system has translation invariance along the x direction. According to Young's relation, the geometric relation between the cylinder surface and the meniscus is given by

$$\phi_l = \varphi_l + \theta, \tag{2.3}$$

where the angles $\phi_l = \pi/2 - \psi_l$ and φ_l are measured clockwise, with reference to figure 1(*c*), starting from the horizontal line, to the unit normal vectors $\boldsymbol{n}_m$ and $\boldsymbol{n}_s$, of the meniscus and the cylinder surface at the left contact point, respectively. The cylinder surface is expressed by the parametric function $\boldsymbol{r}(t) = [x(t), y(t)]$, where the parametric expression is the same as that in Kemp & Siegel (2011). Meanwhile, the position and orientation of the cylinder are determined by $\boldsymbol{r}(t)$. It is assumed that the parametrization is oriented counterclockwise and the derivative $\boldsymbol{r}'(t)$ is never $\boldsymbol{0}$. The position vector of the left contact point is denoted by $\boldsymbol{r}(t_l)$. According to the geometric relation at the left contact point, the parameter t_l and the angles φ_l and ψ_l are related by

$$x'(t_l) = \tan \varphi_l y'(t_l) \quad \text{and} \quad y(t_l) = u_l, \tag{2.4a,b}$$

where the primes refer to derivatives $\mathrm{d}/\mathrm{d}t$ with respect to the parameter t. Since the cross-section is convex, equations (2.2)–(2.4) have a unique solution $\boldsymbol{r}(t_l)$ for a specific contact angle θ and a specific geometry $\boldsymbol{r}(t)$ (see appendix A).

For the case of the right side, the equations used to determine $\boldsymbol{r}(t_r)$ can be obtained by simply replacing the subscript l with the subscript r in (2.2)–(2.4), and modifying (2.4*a*) to

$$x'(t_r) = -\tan\varphi_r y'(t_r). \tag{2.5}$$

The angles ϕ_r and φ_r are measured counterclockwise. The subscript l means that the quantities are measured at the left contact point while the subscript r corresponds to the right contact point.

When the contact angle θ and the shape of the cross-section are given, the position vectors $\boldsymbol{r}(t_l)$ and $\boldsymbol{r}(t_r)$ and the corresponding angles φ are uniquely determined by the position and orientation of the cylinder. The six quantities x_l, x_r, u_l, u_r, φ_l and φ_r are called basic geometric quantities in the model, because they can be uniquely determined by the geometric constraints.

2.2. *Forces*

When the contact points are obtained from the position and orientation of the cylinder, the configuration is determined. The resultant force $\boldsymbol{f}_{net}$ acting on the cylinder can be given by

$$\boldsymbol{f}_{net} = \boldsymbol{f}_t^l + \boldsymbol{f}_t^r + \boldsymbol{f}_p + \boldsymbol{B} + \boldsymbol{G}. \tag{2.6}$$

The surface tension forces $\boldsymbol{f}_t^l$ and $\boldsymbol{f}_t^r$ at the left and right contact points are

$$\boldsymbol{f}_t^l = -\sigma(\sin\phi_l \boldsymbol{e}_i + \cos\phi_l \boldsymbol{e}_j) \quad \text{and} \quad \boldsymbol{f}_t^r = \sigma(\sin\phi_r \boldsymbol{e}_i - \cos\phi_r \boldsymbol{e}_j), \tag{2.7a,b}$$

respectively. The force $\boldsymbol{P}$ due to the pressure p can be given by the integral over the wetted cylinder surface S_w:

$$\boldsymbol{P} = \int_{S_w} -p\boldsymbol{n}_s \, \mathrm{d}s = \int_{S_w} \rho g y \boldsymbol{n}_s \, \mathrm{d}s. \tag{2.8}$$

However, the expression (2.8) is inconvenient to actually apply to calculation. By applying Green's theorem to (2.8), the force $\boldsymbol{P}$ can be rewritten as

$$\int_{S_w} \rho g y \boldsymbol{n}_s \, \mathrm{d}s = \rho g V_B \boldsymbol{e}_j + \int_{L_c} p_c \boldsymbol{n}_c \, \mathrm{d}l, \tag{2.9}$$

where V_B denotes the area of the shaded section in figure 1(*b*) (i.e. the section submerged in the liquid), and $p_c = \rho g y$ is the compensating pressure on the straight line L_c between the contact points with the unit normal vectors $\boldsymbol{n}_c$ of L_c directed inward toward the shaded section. Equation (2.9) expresses the decomposition of the force $\boldsymbol{P}$ into the compensating pressure force $\boldsymbol{f}_p$ and the buoyancy force $\boldsymbol{B}$, while there is another decomposition of $\boldsymbol{P}$ adopted in, e.g. Keller (1998). Keller (1998) calculated the pressure force $\boldsymbol{P}$ by directly integrating p over the wetted cylinder surface. Results shown that the vertical component of $\boldsymbol{P}$ is equal to the weight of the liquid that occupies the volume whose boundaries comprise the undisturbed interface, the vertical lines between the contact points and the undisturbed interface and the wetted surface of the cylinder (Keller 1998). The two methods of decomposition are equivalent from the point of view of force. The force $\boldsymbol{f}_p$ can be obtained by integrating $p_c \boldsymbol{n}_c$ on the line, given by

$$\boldsymbol{f}_p = \frac{\rho g}{2}[(u_r^2 - u_l^2)\boldsymbol{e}_i - (x_r - x_l)(u_l + u_r)\boldsymbol{e}_j], \tag{2.10}$$

where the first vector on the right-hand side of (2.10) is equal to the horizontal component of the pressure force provided by Keller (1998).

The horizontal resultant force on the cylinder is the sum of the horizontal components of the forces $\boldsymbol{f}_p$, $\boldsymbol{f}_t^l$ and $\boldsymbol{f}_t^r$:

$$f_{net}^h = \sigma \left[\frac{\kappa}{2}(u_r^2 - u_l^2) + (\sin \phi_r - \sin \phi_l) \right]. \tag{2.11}$$

Using (2.1), it is found that the horizontal force f_{net}^h is always zero, which means that the horizontal equilibrium condition is automatically satisfied. The horizontal resultant force induced by the surface tension imbalance has been investigated by Janssens, Chaurasia & Fried (2017). From (2.6), (2.7) and (2.10), the vertical resultant force,

$$f_{net}^v = -\frac{\rho g}{2}(x_r - x_l)(u_l + u_r) - \sigma(\cos \phi_r + \cos \phi_l) + \rho g V_B - mg, \tag{2.12}$$

can be calculated with the position vectors of the contact points $\boldsymbol{r}(t_l) = (x_l, u_l)$ and $\boldsymbol{r}(t_r) = (x_r, u_r)$, and the angles ϕ_l and ϕ_r, where m is the mass of the cylinder. As discussed in the previous section, the basic geometric quantities depend only on the position and orientation of the cylinder. Thus, when the contact angle and the shape of the cross-section are given, the resultant force can be calculated from the position and orientation of the cylinder.

2.3. *Vertical equilibrium and stability*

After determining the relation between the resultant force and the position and orientation of the cylinder, the next step is to find the equilibrium position. However, it is inconvenient to calculate the equilibrium position by solving $f_{net}^v = 0$ directly, because the expression for V_B in (2.12) is difficult to determine without a given cross-section. An alternative is to calculate the force variation δf_{net}^v corresponding to an infinitesimal displacement δh in height of the cylinder with a fixed orientation and a given height h^* (see figure 2a), and then to use the function $\delta f_{net}^v/\delta h$ and the force f_{net}^v given by (2.12) as the ordinary differential equation and the initial condition, respectively, to form an initial value problem (IVP):

$$\left.\begin{aligned} \dot{f} &= \delta f_{net}^v/\delta h, \\ f(h^*) &= f_{net}^v, \end{aligned}\right\} \tag{2.13}$$

where h denotes the height of the cylinder measured from the undisturbed liquid surface and a dot over a character denotes the derivative of the corresponding displacement. It is noted that all the variations in the model are considered in the context of the principle of virtual work dating back to Bernoulli. The reference point p_h for determining the height h can be any point, e.g. the centroid of the cross-section. This problem has a unique solution, which means that the vertical force f_{net}^v is entirely determined by the height h. The vertical equilibria can be obtained from the force profile, and their stabilities can be determined by the derivatives $\dot{f}$, where $\dot{f} < 0$ and $\dot{f} > 0$ correspond to stable and unstable equilibria, respectively.

Because the weight force $\boldsymbol{G}$ is constant, the variation of the net force f_{net}^v is deduced from (2.12) as

$$\begin{aligned} \delta f_{net}^v = {}& -\frac{\rho g}{2}[(u_l + u_r)(\delta x_r - \delta x_l) + (x_r - x_l)(\delta u_l + \delta u_r)] \\ & + \sigma(\sin \phi_l \delta \varphi_l + \sin \phi_r \delta \varphi_r) + \rho g \delta V_B. \end{aligned} \tag{2.14}$$
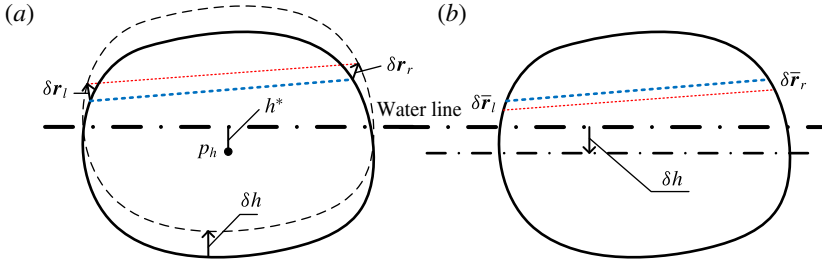
FIGURE 2. (Colour online) An infinitesimal displacement in h results in the displacement of the contact points: (a) δr_l and δr_r for the reference frame fixed in the liquid, and (b) $\delta \bar{r}_l$ and $\delta \bar{r}_r$ for the reference frame fixed in the solid. The point p_h is the reference point for the height h. The horizontal thick dot-dash line and the horizontal thin dot-dash line are the water lines before and after the displacement of the cylinder, respectively. The blue thick and red thin dashed lines are the lines L_c before and after the displacement of the cylinder, respectively.

The variations $(\delta x_l, \delta u_l)$, $\delta \varphi_l$ and δV_B to the first order in δh are shown as

$$\delta x_l = -\frac{\sqrt{\kappa} R_l \sin \varphi_l}{\sqrt{\kappa} R_l \cos \varphi_l + \sin \left(\dfrac{\varphi_l + \theta}{2} + \dfrac{\pi}{4} \right)} \delta h, \tag{2.15a}$$

$$\delta u_l = \frac{\sin \left(\dfrac{\varphi_l + \theta}{2} + \dfrac{\pi}{4} \right)}{\sqrt{\kappa} R_l \cos \varphi_l + \sin \left(\dfrac{\varphi_l + \theta}{2} + \dfrac{\pi}{4} \right)} \delta h, \tag{2.15b}$$

$$\delta \varphi_l = -\frac{\sqrt{\kappa}}{\sqrt{\kappa} R_l \cos \varphi_l + \sin \left(\dfrac{\varphi_l + \theta}{2} + \dfrac{\pi}{4} \right)} \delta h, \tag{2.15c}$$

$$\delta V_B = \tfrac{1}{2} [(u_l - u_r)(\delta x_r + \delta x_l) + (x_r - x_l)(\delta u_l + \delta u_r - 2\delta h)], \tag{2.15d}$$

where R_l denotes the radius of curvature at the left contact point. In the following sections, the variations corresponding to δh are expressed to the first order in δh. The variations $(\delta x_r, \delta u_r)$ and $\delta \varphi_r$ are determined by replacing the subscript l with r in (2.15a–c), and modifying (2.15a) to

$$\delta x_r = \frac{\sqrt{\kappa} R_r \sin \varphi_r}{\sqrt{\kappa} R_r \cos \varphi_r + \sin \left(\dfrac{\varphi_r + \theta}{2} + \dfrac{\pi}{4} \right)} \delta h. \tag{2.16}$$

Thus, the differential equation $\dot{f}$ in (2.13) is related to the eight quantities at the contact points: x_l, x_r, u_l, u_r, φ_l, φ_r, R_l and R_r. Accordingly, an IVP in six dimensions is formed to calculate the basic geometric quantities. The radii of curvature R_l and R_r can be determined by the basic geometric quantities and the height h. The IVP for the basic geometric quantities consists of the system of equations: six ODEs and the corresponding initial conditions. For instance, the ODE for x_l is $\dot{x}_l = \delta x_l / \delta h$ together with the initial condition $x_l(h^*) = x_l^*$. By solving the above IVP, the values of the

quantities in (2.13) are obtained. Therefore the resultant force profile can be obtained by solving the system of ODEs together with the initial conditions:

$$\left.\begin{array}{l} \dot{f} = \delta f_{net}^v/\delta h, \ \dot{x}_l = \delta x_l/\delta h, \ \ldots, \ \dot{\varphi}_r = \delta \varphi_r/\delta h, \\ f(h^*) = f_{net}^v, \ x_l(h^*) = x_l^*, \ \ldots, \ \varphi_r(h^*) = \varphi_r^*, \end{array}\right\} \quad (2.17)$$

where the omissions are the ODEs for the basic geometric quantities not shown and the corresponding initial conditions. A detailed description on the derivations of (2.15a–d) is provided in appendix B.

In order to validate the model, the force profile of a uniform cylinder floating in an unbounded bath is obtained by using our numerical code. For simplicity, the Euler method is adopted to solve (2.17). The force analysis of this configuration was given by Princen (1969), who derived an equilibrium equation for a uniform cylinder floating on a liquid surface. Following Princen (1969), Rapacchietta *et al.* (1977) developed a non-equilibrium model and provided the analytical expression of the resultant forces exerted on a uniform cylinder. The numerical result in this paper is compared to the analytical expression presented by Rapacchietta *et al.* (1977). The resultant force exerted on the uniform cylinder is given by

$$\begin{aligned} f_{net}^v = {}& -2\sigma \cos(\theta + \varphi_r) - mg \\ & + \rho g r^2 \left\{ \varphi_r + \frac{\pi}{2} - \cos \varphi_r \left[\frac{4}{\sqrt{\kappa} r} \cos \left(\frac{\theta + \varphi_r}{2} + \frac{\pi}{4} \right) - \sin \varphi_r \right] \right\}, \quad (2.18) \end{aligned}$$

where r denotes the radius of the cylinder.

Figure 3(*a*) compares the numerical result to the analytical solution of Rapacchietta *et al.* (1977) for a uniform cylinder. The inset shows the relative error of the numerical simulation. An excellent agreement is found, demonstrating the validity of our numerical code for the force profile of the cylinder. We assume that all configurations are in equilibrium, i.e. the mass of the cylinder is given as a function of the position of the cylinder to counteract the other forces. During the numerical simulation, the stability in the vertical direction can easily be obtained from the first derivative of the force, as shown in figure 3(*b*). A theoretical stability analysis for this case was conducted by Bhatnagar & Finn (2006), who solved an eigenvalue problem associated with the second variation of energy to predict the vertical stability of the cylinder. Following the approach of Bhatnagar & Finn (2006) with some modifications, Chen & Siegel (2018) predicted the vertical stability by using the relation between the total energy and the resultant force.

In the mathematical model, the variation of the resultant force is described as a function of the basic geometric quantities and their variations, transforming a number of irrelevant and repetitive problems of solving the resultant force in one problem similar to the IVP. The advantages of this model are that it avoids repetition of § 2.1 for determining the configurations in which the menisci satisfy the Young–Laplace equation with Young's relation, and transforms the change of the configuration to the variations of the basic geometric quantities: δx_l, δx_r, δu_l, δu_r, $\delta \varphi_l$ and $\delta \varphi_r$. Thus, the complex configurations can be obtained by integrating a simple configuration. For instance, the cylinder floating in an infinite bath without gravity (see Kemp & Siegel (2011)) can be used as the initial configuration in the model. The simulations for other cases are shown in § 3.
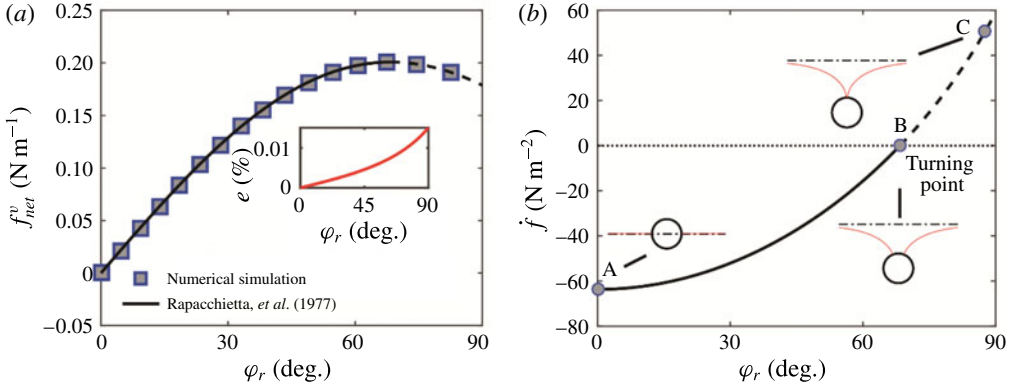
FIGURE 3. (Colour online) (*a*) Comparison between the numerical result and the analytical solution in Rapacchietta *et al.* (1977). The following values of parameters are used: $r = 1.5$ mm, $\theta = \pi/2$, $\sigma = 0.072$ N m^{-1}, $g = 9.81$ m s^{-2}, $\rho = 1000$ kg m^{-3}, $m = \rho\pi r^2/2$ and $\delta h = -3.75 \times 10^{-7}$ m. In the following calculations, the values of ρ, g and σ remain constant. The inset shows the relative error of the numerical simulation. (*b*) The first derivative of force indicates the stability of the cylinder, where A is a stable point, C is an unstable point and B is the turning point. The typical configurations are presented, where the red curves are menisci, the circles are cylinders and the dot-dash lines are water lines.

2.4. *Rotational equilibrium and stability*

When a vertical equilibrium is achieved, the forces with a resultant moment on the cylinder form a couple, which has the same moment $\boldsymbol{M}$ about all points. Thus, the reference point of the resultant moment can be any point. Selecting the origin $\boldsymbol{0}$ as the reference point, the moment can be given by

$$\boldsymbol{M} = \boldsymbol{r}_l \times \boldsymbol{f}_t^l + \boldsymbol{r}_r \times \boldsymbol{f}_t^r + \boldsymbol{r}_p \times \boldsymbol{f}_p + \boldsymbol{r}_B \times \boldsymbol{B} + \boldsymbol{r}_G \times \boldsymbol{G}, \tag{2.19}$$

where $\boldsymbol{r}_p$, $\boldsymbol{r}_B$ and $\boldsymbol{r}_G$ denote the position vectors of $\boldsymbol{f}_p$, $\boldsymbol{B}$ and $\boldsymbol{G}$, respectively. The position vector $\boldsymbol{r}_p$ depends on the two vectors $\boldsymbol{r}_l$ and $\boldsymbol{r}_r$ as:

$$\boldsymbol{r}_p = \xi_l \boldsymbol{r}_l + \xi_r \boldsymbol{r}_r, \tag{2.20}$$

where

$$\xi_l = \frac{2u_l + u_r}{3u_l + 3u_r} \quad \text{and} \quad \xi_r = \frac{u_l + 2u_r}{3u_l + 3u_r}. \tag{2.21a,b}$$

We suppose that the shaded area V_B, the mass m and their centres $\boldsymbol{r}_B$ and $\boldsymbol{r}_G$ in figure 1(*b*) have been determined from the cross-section and the contact points $\boldsymbol{r}_l$ and $\boldsymbol{r}_r$. The moment $\boldsymbol{M}$ can be calculated by (2.19).

To deal with the rotational equilibria, we will use an analogous approach to § 2.3 to obtain the moment profile $\boldsymbol{M}(\varepsilon)$. By rotating the cylinder counterclockwise around the point p_{ro} by an infinitesimally small angle $\delta\varepsilon$ (see figure 4*a*), the change in the moment can be divided into four parts:

$$\delta\boldsymbol{M} = \delta\boldsymbol{M}_t + \delta\boldsymbol{M}_p + \delta\boldsymbol{M}_B + \delta\boldsymbol{M}_G, \tag{2.22}$$
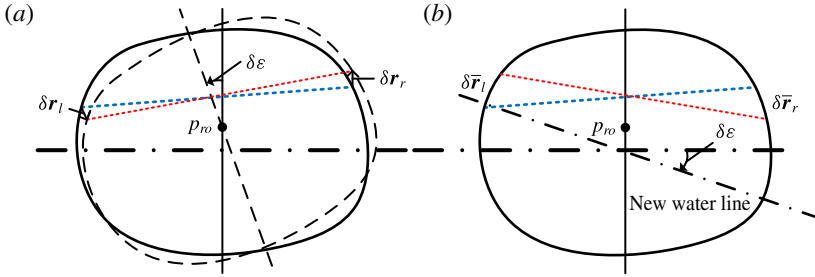
FIGURE 4. (Colour online) An infinitesimal rotation $\delta\varepsilon$ results in the displacement of the contact points: (*a*) $\delta\boldsymbol{r}_l$ and $\delta\boldsymbol{r}_r$ for the reference frame fixed in the liquid, and (*b*) $\delta\bar{\boldsymbol{r}}_l$ and $\delta\bar{\boldsymbol{r}}_r$ for the reference frame fixed in the solid. The point p_{ro} is the instantaneous centre of rotation. The inclined black thin dot-dash line in (*b*) is the water line after the rotation $\delta\varepsilon$. The blue thick and red thin dashed lines are the lines L_c before and after the rotation of the cylinder, respectively.

where

$$\delta\boldsymbol{M}_t = \delta\boldsymbol{r}_l \times \boldsymbol{f}_t^l + \delta\boldsymbol{r}_r \times \boldsymbol{f}_t^r + \boldsymbol{r}_l \times \delta\boldsymbol{f}_t^l + \boldsymbol{r}_r \times \delta\boldsymbol{f}_t^r, \quad (2.23a)$$

$$\delta\boldsymbol{M}_p = \delta(\boldsymbol{r}_p \times \boldsymbol{f}_p), \quad (2.23b)$$

$$\delta\boldsymbol{M}_B = \delta\boldsymbol{r}_B \times \boldsymbol{B} + \boldsymbol{r}_B \times \delta\boldsymbol{B}, \quad (2.23c)$$

$$\delta\boldsymbol{M}_G = \delta\boldsymbol{r}_G \times \boldsymbol{G}, \quad (2.23d)$$

are the moment variations due to the surface tension force, the compensating pressure force, the buoyancy and the weight force, respectively.

Utilizing the same method as in §2.3, an IVP to calculate the resultant moment $\boldsymbol{M}$ is formed as follows:

$$\left.\begin{aligned} \dot{M} &= \delta M/\delta\varepsilon, \\ M(0) &= M_{in}, \end{aligned}\right\} \quad (2.24)$$

where M is the scalar projection of $\boldsymbol{M}$ in the direction of the z axis, and the subscript *in* denotes the initial condition. For simplicity, the resultant moment $\boldsymbol{M}$ refers to its vector projection M, because the other scalar projections are zero. The rotational equilibria can be obtained from the moment profile, and their stabilities can be determined by the derivatives $\dot{M}$, where $\dot{M} < 0$ and $\dot{M} > 0$ correspond to stable and unstable equilibria, respectively.

To keep the resultant moment M about any reference point constant, the force variation δf_{net}^v corresponding to the infinitesimal displacement $\delta\varepsilon$ must be $o(\delta\varepsilon)$ during rotation. From (2.14), the variation δf_{net}^v can be expressed in terms of the variations $\delta\boldsymbol{r}_l$, $\delta\boldsymbol{r}_r$, $\delta\varphi_l$, $\delta\varphi_r$ and δV_B, which are linearly related to the rotational displacement $\delta\varepsilon$:

$$\delta x_l = \left[\frac{\sqrt{\kappa}\cos\varphi_l L_l + \sin\left(\dfrac{\varphi_l + \theta}{2} + \dfrac{\pi}{4}\right)}{\sqrt{\kappa}\cos\varphi_l R_l + \sin\left(\dfrac{\varphi_l + \theta}{2} + \dfrac{\pi}{4}\right)} \sin\varphi_l R_l - (u_l - u_{ro}) \right] \delta\varepsilon, \quad (2.25a)$$

$$\delta u_l = \frac{\sin\left(\dfrac{\varphi_l + \theta}{2} + \dfrac{\pi}{4}\right)\cos\varphi_l(R_l - L_l)}{\sqrt{\kappa}\cos\varphi_l R_l + \sin\left(\dfrac{\varphi_l + \theta}{2} + \dfrac{\pi}{4}\right)}\delta\varepsilon, \tag{2.25b}$$

$$\delta\varphi_l = -\frac{\sqrt{\kappa}\cos\varphi_l(R_l - L_l)}{\sqrt{\kappa}\cos\varphi_l R_l + \sin\left(\dfrac{\varphi_l + \theta}{2} + \dfrac{\pi}{4}\right)}\delta\varepsilon, \tag{2.25c}$$

$$\begin{aligned}\delta V_B =\ & \tfrac{1}{2}[(u_l - u_r)(\delta x_r + \delta x_l) + (x_r - x_l)(\delta u_l + \delta u_r)] \\ & + \tfrac{1}{2}[(u_l - u_r)(u_r + u_l - 2u_{ro}) + (x_l - x_r)(x_l + x_r - 2x_{ro})]\delta\varepsilon, \end{aligned} \tag{2.25d}$$

where $L_l = (x_{ro} - x_l)/\cos\varphi_l$ denotes the length of the line segment parallel to $\boldsymbol{n}_s$ bounded by the vertical lines $x = x_{ro}$ and $x = x_l$. For the case on the right side, the variations $(\delta x_r, \delta u_r)$ and $\delta\varphi_r$ are determined by replacing the subscript l with r in (2.25a–c), and modifying (2.25b,c) to

$$\delta u_r = -\frac{\sin\left(\dfrac{\varphi_r + \theta}{2} + \dfrac{\pi}{4}\right)\cos\varphi_r(R_r - L_r)}{\sqrt{\kappa}R_r\cos\varphi_r + \sin\left(\dfrac{\varphi_r + \theta}{2} + \dfrac{\pi}{4}\right)}\delta\varepsilon, \tag{2.26a}$$

$$\delta\varphi_r = \frac{\sqrt{\kappa}\cos\varphi_r(R_r - L_r)}{\sqrt{\kappa}\cos\varphi_r R_r + \sin\left(\dfrac{\varphi_r + \theta}{2} + \dfrac{\pi}{4}\right)}\delta\varepsilon, \tag{2.26b}$$

where $L_r = -(x_{ro} - x_r)/\cos\varphi_r$.

Substituting in (2.14) for the variations of the basic geometric quantities and the area δV_B given by (2.25a–d) and (2.26a,b), a straightforward but tedious calculation gives

$$x_{ro} = \frac{\rho g\eta/2 + \xi_l(x_l + \cos\varphi_l R_l) + \xi_r(x_r + \cos\varphi_r R_r)}{\rho g(x_r - x_l + u_l\tan\varphi_l + u_r\tan\varphi_r) + \xi_l + \xi_r}, \tag{2.27}$$

where

$$\eta = x_r^2 - x_l^2 - u_r^2 + u_l^2 + 2\tan\varphi_l x_l u_l + 2\tan\varphi_r x_r u_r, \tag{2.28a}$$

$$\xi_l = \frac{\sqrt{\kappa}\sigma\sin(\varphi_l + \theta) - \rho g u_l\sin\left(\dfrac{\varphi_l + \theta}{2} + \dfrac{\pi}{4}\right)\tan\varphi_l}{\sqrt{\kappa}\cos\varphi_l R_l + \sin\left(\dfrac{\varphi_l + \theta}{2} + \dfrac{\pi}{4}\right)}, \tag{2.28b}$$

$$\xi_r = \frac{\sqrt{\kappa}\sigma\sin(\varphi_r + \theta) - \rho g u_r\sin\left(\dfrac{\varphi_r + \theta}{2} + \dfrac{\pi}{4}\right)\tan\varphi_r}{\sqrt{\kappa}\cos\varphi_r R_r + \sin\left(\dfrac{\varphi_r + \theta}{2} + \dfrac{\pi}{4}\right)}. \tag{2.28c}$$

From the solution (2.27) of $\delta f_{net}^v = 0$, it is found that the height u_{ro} of the rotation centre p_{ro} has no effect on the balance of the vertical force which accounts for the first-order accuracy in $\delta\varepsilon$ in the model. Under this condition, the height u_{ro} only leads

to the horizontal displacement of the cylinder. For the same reason, u_{ro} has no effect on the moment M and its variation δM, and then u_{ro} could be given as zero for the following calculations.

After determining the instant rotation centre (x_{ro}, u_{ro}), the basic geometric quantities can be obtained by integrating the initial conditions, where the numerical methods used are the same as those in § 2.3.

Referring to (2.22), the variation δM consists of δM_t, δM_p, δM_B and δM_G, which can be respectively given by:

$$\delta M_t = \sigma \cos(\varphi_l + \theta)(u_l \delta \varphi_l - \delta x_l) + \sigma \sin(\varphi_l + \theta)(x_l \delta \varphi_l + \delta u_l)$$
$$- \sigma \cos(\varphi_r + \theta)(u_r \delta \varphi_r + \delta x_r) + \sigma \sin(\varphi_r + \theta)(x_r \delta \varphi_r - \delta u_r), \quad (2.29a)$$

$$\delta M_p = \frac{\rho g}{6} \left[(6u_l^2 + 2x_l^2 - x_l x_r - x_r^2)\delta u_l - (6u_r^2 + 2x_r^2 - x_l x_r - x_l^2)\delta u_r \right.$$
$$\left. + (4x_l u_l + 2x_l u_r - x_r u_l + x_r u_r)\delta x_l - (4x_r u_r + 2x_r u_l - x_l u_r + x_l u_l)\delta x_r \right], \quad (2.29b)$$

$$\delta M_B = \rho g[\delta S_y - V_B(u_B - u_{ro})\delta \varepsilon], \quad (2.29c)$$

$$\delta M_G = -(u_G - u_{ro})mg\delta \varepsilon, \quad (2.29d)$$

where δS_y denotes the first moment of the area of the quadrilateral *ABCD* in the y direction, where the position vectors of four vertices of the quadrilateral *ABCD* are $\boldsymbol{r}_l$, $\boldsymbol{r}_r$, $\boldsymbol{r}_r + \delta \tilde{\boldsymbol{r}}_r$ and $\boldsymbol{r}_l + \delta \tilde{\boldsymbol{r}}_l$. A tilde over a character designates a quantity measured on the reference frame of the cylinder after rotation. Then, two IVPs in two dimensions are formed to calculate the position vectors $\boldsymbol{r}_B$ and $\boldsymbol{r}_G$, where two systems of ODEs are constructed by

$$\left. \begin{array}{l} \dot{x}_B \equiv \dfrac{\delta x_B}{\delta \varepsilon} = \dfrac{\delta S_y - x_B \delta V_B}{V_B \delta \varepsilon} - (u_B - u_{ro}), \\[3mm] \dot{u}_B \equiv \dfrac{\delta u_B}{\delta \varepsilon} = \dfrac{\delta S_x - u_B \delta V_B}{V_B \delta \varepsilon} + (x_B - x_{ro}), \end{array} \right\} \quad (2.30)$$

$$\left. \begin{array}{l} \dot{x}_G \equiv \dfrac{\delta x_G}{\delta \varepsilon} = -(u_G - u_{ro}), \\[3mm] \dot{u}_G \equiv \dfrac{\delta u_G}{\delta \varepsilon} = (x_G - x_{ro}), \end{array} \right\} \quad (2.31)$$

where

$$\delta S_y = \tfrac{1}{6} \left[(x_r^2 + x_l x_r - 2x_l^2)\delta \tilde{u}_l - (x_r x_l + x_l^2 - 2x_r^2)\delta \tilde{u}_r \right.$$
$$\left. + (2x_l u_l + x_r u_l - 2x_l u_r - x_r u_r)\delta \tilde{x}_l - (2x_r u_r + x_l u_r - 2x_r u_l - x_l u_l)\delta \tilde{x}_r \right], \quad (2.32a)$$

$$\delta S_x = \tfrac{1}{6} \left[(2u_l^2 - u_l u_r - u_r^2)\delta \tilde{x}_l - (2u_r^2 - u_r u_l - u_l^2)\delta \tilde{x}_r \right.$$
$$\left. + (2x_r u_l + x_r u_r - 2x_l u_l - x_l u_r)\delta \tilde{u}_l - (2x_l u_r + x_l u_l - 2x_r u_r - x_r u_l)\delta \tilde{u}_r \right], \quad (2.32b)$$

with the variations

$$\left. \begin{array}{l} \delta \tilde{x}_l = \delta x_l + (u_l - u_{ro})\delta \varepsilon, \\[1mm] \delta \tilde{x}_r = \delta x_r + (u_r - u_{ro})\delta \varepsilon, \\[1mm] \delta \tilde{u}_l = \delta u_l - (x_l - x_{ro})\delta \varepsilon, \\[1mm] \delta \tilde{u}_r = \delta u_r - (x_r - x_{ro})\delta \varepsilon. \end{array} \right\} \quad (2.33)$$

Similar to the model for the vertical displacement, the variations of all quantities are expressed to the first order of $\delta \varepsilon$, and then the IVPs are formed to calculate

the corresponding quantities. Before constructing the IVPs, the instant rotation centre p_{ro} is determined by (2.27) to keep the vertical equilibrium of the cylinder. So, the moment will not change with the location of the reference point of moment. For the initial conditions, the quantities for determining the initial configuration need to be given, including r_l, r_r, r_B, r_G, φ_l, φ_r and V_B. These quantities can be used to determine the resultant moment M and the radii of the curvature R_l and R_r.

In the model, the calculation of the resultant moment M can be performed in four steps. First, an IVP is formed by (2.25a–c) and (2.26a,b) with initial conditions and then is solved for calculating the basic geometric quantities in the process of rotation. Second, the area V_B is calculated by integrating (2.25d) in the same way. Then the vector positions r_B and r_G are determined by solving the two systems of ODEs (2.30) and (2.31) with initial conditions. Finally, the differential function $\dot{M}$ is obtained by substituting equations (2.29a–d) into (2.24) and then is solved for determining the rotational equilibria and their stabilities. The derivations of the variations δr_l, δr_r, $\delta \varphi_l$, $\delta \varphi_r$, δV_B and δM are provided in appendix C. Analogous expressions of $\dot{f}$ and $\dot{M}$ for axisymmetric floating bodies have been obtained by Huh & Mason (1974). However, the derivative $\dot{M}$ cannot be used to calculate M.

3. Results and discussion

In this section, cylinders with several cross-sections are investigated using our model for the vertical and rotational equilibria and their stabilities. Then the surface tension effects on the vertical and rotational stabilities are investigated by varying the following parameters: the radii of curvature of the solid surface at contact points and the size of floating body.

3.1. *Cylinders of different cross-section shapes*

3.1.1. *Ellipse*

The elliptical cross-section shape is expressed as the parametric equation

$$r(t) = (a \cos t, b \sin t + h^*) \quad \text{for } t \in [0, 2\pi] \tag{3.1}$$

with a, $b > 0$. The parametric equation can determine the initial conditions with a specified contact angle θ. To simplify the problem, configurations without gravity are used as the initial conditions in the model, where the menisci around the cylinder are flat. To keep the menisci flat, the height h^* and the contact angle θ satisfy the relation:

$$\cos \theta + \frac{ah^*}{\sqrt{(ah^*)^2 - (bh^*)^2 + b^4}} = 0. \tag{3.2}$$

The height h^* can be obtained by solving equation (3.2). As presented in §2.3, the basic geometric quantities are used as the initial conditions in the model of the vertical displacement, which are expressed in terms of the parameters h^* and θ:

$$\left.\begin{aligned} x_l &= -\frac{a}{b}\sqrt{b^2 - h^{*2}}, \\ x_r &= \frac{a}{b}\sqrt{b^2 - h^{*2}}, \end{aligned}\right\} \quad \left.\begin{aligned} u_l &= 0 \\ u_r &= 0 \end{aligned}\right\} \quad \text{and} \quad \left.\begin{aligned} \varphi_l &= \frac{\pi}{2} - \theta, \\ \varphi_r &= \frac{\pi}{2} - \theta. \end{aligned}\right\} \tag{3.3a–c}$$

Then configurations varying with h can be obtained by solving the model.

In our model, the radii of curvature are the only parameters directly related to the shape of cross-section. After determining the radii of curvature corresponding to different cross-sections, the corresponding configurations can be calculated. For elliptical cross-sections, the radii of curvature are determined by:

$$R = \frac{(a^2 \sin^2 t + b^2 \cos^2 t)^{3/2}}{ab}, \tag{3.4}$$

where

$$\frac{a}{b} \tan t_l = \tan(\pi - \bar{\varphi}_l) \quad \text{and} \quad \frac{a}{b} \tan t_r = \tan \bar{\varphi}_r, \tag{3.5a,b}$$

with

$$\left.\begin{array}{l} \bar{\varphi}_l = \varphi_l, \\ \bar{\varphi}_r = \varphi_r, \end{array}\right\} \tag{3.6a}$$

for the vertical displacement and

$$\left.\begin{array}{l} \bar{\varphi}_l = \varphi_l + \varepsilon, \\ \bar{\varphi}_r = \varphi_r - \varepsilon, \end{array}\right\} \tag{3.6b}$$

for the rotational displacement, where the bar over the character designates the quantity measured on the reference frame of the cylinder before rotation. For simplicity, the contact angles and the resultant forces of the initial configurations are given by $\pi/2$ and 0 for the cases regarding the vertical and rotational displacements, respectively.

Figure 5(*a*) shows the resultant forces varying with h, where the areas of the cross-sections are identical to each other. Results show the higher the ratio $\lambda = a/b$, the greater the maximum resultant force (see the insets A–E) and the lower the height of the corresponding position, which are the same as the results in Liu, Feng & Wang (2007). The maximum resultant forces correspond to the second-order condition $\delta f^v_{net}/\delta h = 0$ for stability. In our model the vertical stability can be obtained directly from (2.13) without plotting the force profile.

For the rotational displacement, the buoyancy, the weight force and their position vectors are needed for the initial conditions:

$$\left.\begin{array}{l} \boldsymbol{B} = \dfrac{\pi ab\rho g}{2} \boldsymbol{e}_j, \\ \boldsymbol{r}_B = -\dfrac{4b}{3\pi} \boldsymbol{e}_j \end{array}\right\} \quad \text{and} \quad \left.\begin{array}{l} \boldsymbol{G} = -\boldsymbol{B}, \\ \boldsymbol{r}_G = \boldsymbol{0}. \end{array}\right\} \tag{3.7a,b}$$

To keep the vertical force balance of the floating cylinder, the rotation centre is calculated by (2.27). In these cases, the contact angles are $\pi/2$, leading to the central symmetry of the configurations. Thus the rotation centres are fixed at $\boldsymbol{0}$ during rotation.

In figure 5(*b*), the moments of the four ellipses with different values of λ are calculated by using our model. The areas of the cross-sections are identical to each other. The cases of λ and $1/\lambda$ are equivalent to each other. There are two rotational equilibria for $\varepsilon \in [0, \pi/2]$, where one equilibrium ($\varepsilon = 0$) is unstable and the other ($\varepsilon = \pi/2$) is stable. The configurations with the maximum resultant moment are shown by the insets F–I. A similar configuration (spheroid) has been investigated theoretically
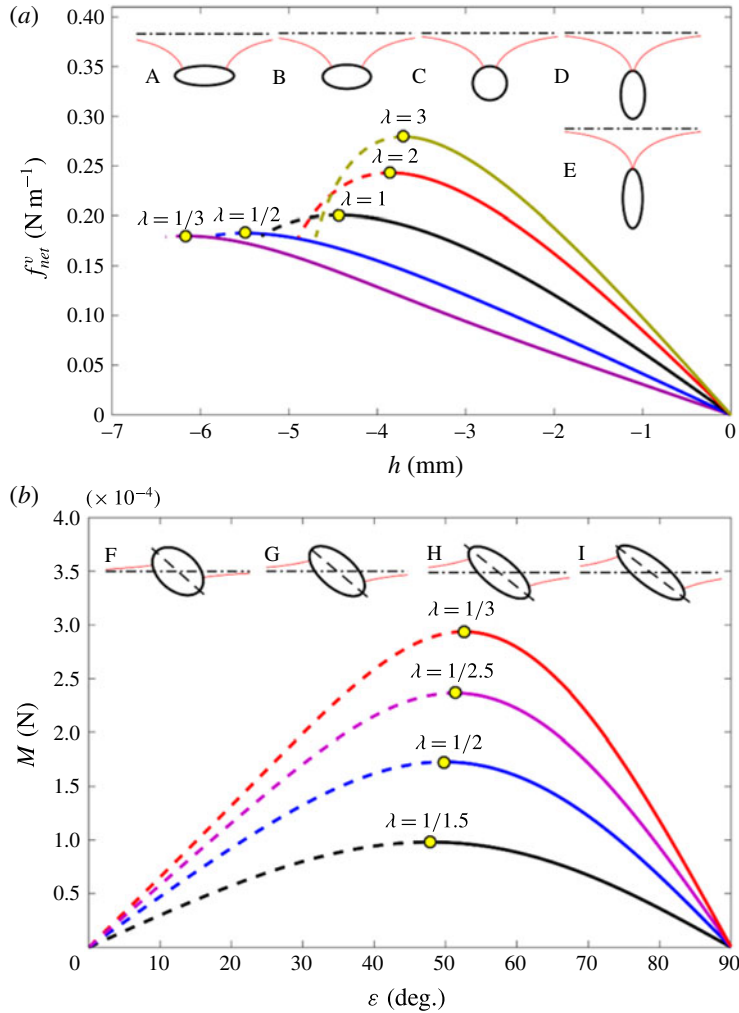
FIGURE 5. (Colour online) (*a*) The resultant forces exerted on the cylinders varying with the height *h* and (*b*) the resultant moments exerted on the cylinders varying with the inclination angle ε. The following values of parameters are used: $\theta = \pi/2$ and $ab = (1.5 \text{ mm})^2$. It is assumed that the cylinders are in equilibrium (vertical and rotational), and then the solid lines correspond to the stable equilibria while the dashed lines correspond to the unstable equilibria. The insets refer to the configurations of different values of λ: A, B, C, D and E correspond to $\lambda = 3, 2, 1, 1/2$ and $1/3$ for vertical translation and F, G, H and I correspond to $\lambda = 1/1.5, 1/2, 1/2.5$ and $1/3$ for rotation, respectively.

by Huh & Mason (1974), and results show a prolate spheroid is rotationally stable whereas an oblate spheroid is unstable. This conclusion for the axisymmetric cases is still consistent with the two-dimensional cases. It can be conjectured that the rotational stability is closely related to the radii of curvature. In §3.2, the effect of the radii of curvature R_l and R_r on the vertical and rotational stabilities will be studied.
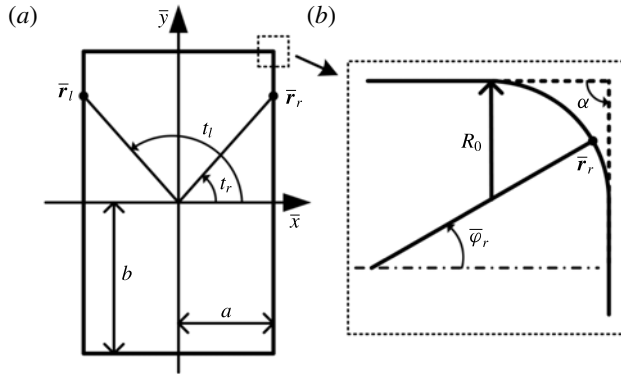
FIGURE 6. Schematics of (*a*) the rectangular cross-section and (*b*) the sharp corner with $\alpha = \pi/2$.

3.1.2. *Rectangle*

Compared to the ellipse, the rectangular cross-section contains four sharp edges, which may lead to the pinning of contact point at the sharp edge, known as the Gibbs inequality condition (Princen 1969; Oliver, Huh & Mason 1977). In this section, rectangular cross-sections are taken as examples to study the edge effect on the vertical and rotational stabilities.

When the contact points lie on the straight line, the polar angles of $\bar{r}_l$ and $\bar{r}_r$ can be used to determine R_l and R_r (see figure 6*a*),

$$\left. \begin{aligned} R_l = \infty, \quad \text{for } |\tan t_l| \neq \frac{b}{a}, \\ R_r = \infty, \quad \text{for } |\tan t_r| \neq \frac{b}{a}, \end{aligned} \right\} \tag{3.8}$$

respectively. However, when the contact points are pinned at the sharp edges, the values of R_l and R_r are uncertain. As discussed in Oliver *et al.* (1977), the sharp edge can be considered as a continuous surface without singularities, which is rounded with $R_0 \to 0$, so that the contact angle remains constant. We suppose that the right contact point is pinned at the sharp edge (see figure 6*b*). When the contact point crosses the edge, the angle $\bar{\varphi}_r$ increases by the angle $\pi - \alpha$. The angle $\bar{\varphi}_r$ before reaching the edge is denoted by $\bar{\varphi}_r^*$, and therefore the radius of curvature at the right contact point is given by

$$\left. \begin{aligned} R_r = 0, \quad \text{for } \bar{\varphi}_r^* < \bar{\varphi}_r < \bar{\varphi}_r^* + \pi - \alpha, \\ R_r = \infty, \quad \text{for } \bar{\varphi}_r = \bar{\varphi}_r^* \text{ and } \bar{\varphi}_r = \bar{\varphi}_r^* + \pi - \alpha. \end{aligned} \right\} \tag{3.9}$$

The case on the left side is the same as that on the right side.

In the case, the initial conditions are given by

$$\left. \begin{aligned} \left. \begin{aligned} x_l = -a, \\ x_r = a, \end{aligned} \right\} \quad \left. \begin{aligned} u_l = \frac{2}{\sqrt{\kappa}} \cos\left(\frac{\theta}{2} + \frac{\pi}{4}\right) \\ u_r = u_l \end{aligned} \right\} \quad \text{and} \quad \left. \begin{aligned} \varphi_l = 0 \\ \varphi_r = 0 \end{aligned} \right\} \\ \text{for } \left| \frac{2}{\sqrt{\kappa}} \cos\left(\frac{\theta}{2} + \frac{\pi}{4}\right) \right| < |b|, \end{aligned} \right\} \tag{3.10}$$

and

$$
\left.
\begin{array}{l}
\left.\begin{array}{l} x_l = -a, \\ x_r = a, \end{array}\right\}
\quad
\left.\begin{array}{l} u_l = \text{sign}\left(\dfrac{\pi}{2} - \theta\right) b \\ u_r = u_l \end{array}\right\}
\quad \text{and} \quad
\left.\begin{array}{l} \varphi_l = 2\cos^{-1}\left(\dfrac{\sqrt{\kappa}\,u_l}{2}\right) - \dfrac{\pi}{2} \\ \varphi_r = \varphi_l \end{array}\right\}
\\[2em]
\text{for } \left|\dfrac{2}{\sqrt{\kappa}}\cos\left(\dfrac{\theta}{2} + \dfrac{\pi}{4}\right)\right| \geqslant |b|.
\end{array}
\right\}
$$

(3.11)

Then the resultant force of the initial configuration can be calculated by (2.12).

Figure 7(*a*) shows the resultant forces acting on the squares varying with the height *h*, which is measured from the water line to the centroids of the squares. The squares ($\lambda = 1$) are selected because the ratio $\lambda = a/b$ has no qualitative effect on the force profiles. The movements of the squares into water can be divided into three stages (denoted by the Roman numerals in figure 7*a*) due to the edge effect. Before the pinning of the contact points, the force profiles are straight lines similar to those without surface tension, because the surface tension forces remain constant in the first stage. When the contact points are attached to the edges, the force profiles are steeper than those of the first stage. Between the first and second stages, the non-smoothness of the force profiles is caused by the discontinuities of δf_t^l and δf_t^r, leading to the increases of the vertical stabilities. In the last stage, the squares reach the maximum depth (see the insets A, B and C), and at the same time the forces decrease dramatically due to the closure of menisci. Force profiles of the squares of the same size are shown for different contact angles. It is shown that the square with greater contact angle can reach a larger depth and bear a bigger pressing force. However, in the second stage all the squares have the same forces at the same depth regardless of the values of the contact angles due to the edge effect.

For the rotational displacement, the force balance conditions must be fulfilled for the initial configuration, which can be easily determined for the upright rectangle. The buoyancy and weight force and their position vectors can be obtained from the initial configuration. Figure 7(*b*) shows the moments varying with the angle ε for a set of squares of the same size with different contact angles and densities. In the range $\varepsilon \in [0, \pi/4]$, there are at least two rotational equilibria, corresponding to $\varepsilon = 0$ and $\varepsilon = \pi/4$, respectively. In the absence of gravity, the stable equilibria for a square exist only when the contact points are pinned at the corners (Kemp & Siegel 2011), implying that the pinned menisci stabilize the square. This result is analogous to figure 7(*b*). Generally, there are five configurations of a rectangle that achieve force balance (see figure 7*b,c*): (i) two contact points lie on the two opposing straight lines; (ii) one contact point is pinned while the other lies on the opposing straight line; (iii) two contact points are pinned at the two opposing straight corners; (iv) two contact points lie on the two adjacent lines; (v) two contact points are pinned at the two neighbouring corners. The derivative of the moment can be used to measure the rotational stability, where the derivative profile is discontinuous between the two stages. It is shown that the configuration with more pinned contact points is more stable. The change from one configuration to another is controlled by many factors, e.g. the ratio of the rectangle, the contact angle, etc. Thus there are many different moment profiles, as shown in figure 7(*b,c*). In figure 7(*c*), results for the rectangles with the ratio $\lambda \neq 1$ are presented, indicating that the ratio λ also has an effect on the rotational equilibria and their stabilities. Results of the rotational displacement for $\varepsilon \in [0, \pi/2]$ are listed in table 1. All of the five typical configurations that achieve
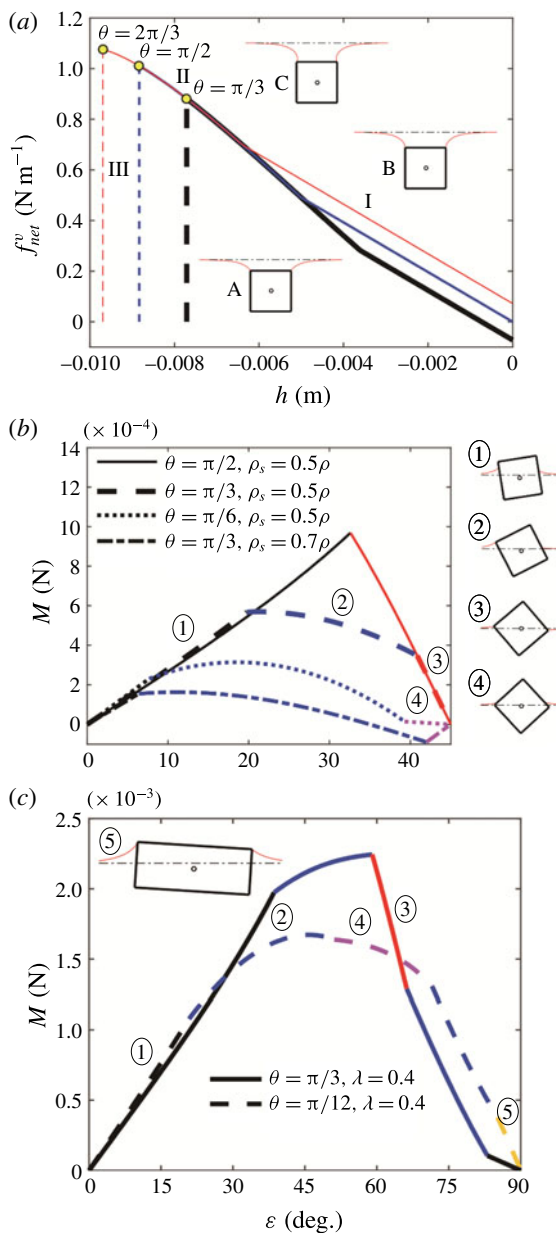
FIGURE 7. (Colour online) (*a*) The resultant force profiles for squares ($\rho_s = 0.5\rho$) with different contact angles, and the resultant moment profiles for (*b*) the squares and (*c*) the rectangles ($\lambda = 0.4$ and $\rho_s = 0.5\rho$) with different contact angles. There are three stages for the vertical displacement denoted by the Roman numerals in (*a*), where the insets denote the configurations that can bear the maximum force: A, B and C corresponding to $\theta = \pi/3$, $\theta = \pi/2$ and $\theta = 2\pi/3$, respectively. In (*b*) and (*c*), five typical configurations for rotational displacement are shown by the insets, where the circles denote centroids, the red lines denote the menisci and the dot-dash lines denote the water lines. All the rectangles have an area of 100 mm^2.
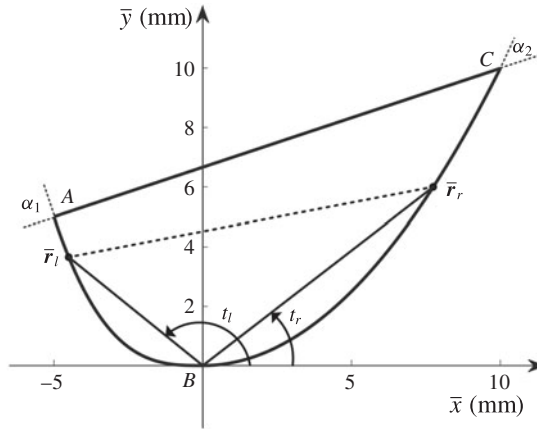
FIGURE 8. Schematic of the selected cross-section with $\alpha_1 = \pi/2$ and $\alpha_2 = \pi/4$.

θ (deg.)	ρ_s	λ	Stable equilibria ε (deg.)	Unstable equilibria ε (deg.)	Progress of rotation
90	0.5ρ	1	45	0, 90	①-③-①
60	0.5ρ	1	45	0, 90	①-②-③-②-①
30	0.5ρ	1	45	0, 90	①-②-④-②-①
60	0.7ρ	1	35, 55	0, 45, 90	①-②-④-②-①
60	0.5ρ	0.4	90	0	①-②-③-②-①
15	0.5ρ	0.4	90	0	①-②-④-②-⑤

TABLE 1. Numerical results for the rotations of the rectangles in figure 7(*b*,*c*).

force balance are obtained, however not all the typical moment profiles are presented here. The number of equilibria and their stabilities will change with the change of parameters, indicating the bifurcation of the system, which is similar to the result in Zhou & Zhang (2017). It is noted that the type of configuration has an important effect on its rotational stability. The detailed analysis of the cause of the various results is beyond the scope of the present paper.

3.1.3. *Selected shape*

In this section, the configuration of a selected shape (see figure 8) is calculated to illustrate that our model is suitable for arbitrary convex shapes. The selected shape consists of three smooth segments ($\widehat{AB}$, $\widehat{BC}$ and $\widehat{CA}$), which can be expressed as follows:

$$\left.\begin{array}{ll} \widehat{AB}: \bar{y} = -40000\bar{x}^3 & \text{for } \bar{x} \in [-0.005, 0], \\ \widehat{BC}: \bar{y} = 100\bar{x}^2 & \text{for } \bar{x} \in [0, 0.01], \\ \widehat{CA}: \bar{y} = (\bar{x} + 0.02)/3 & \text{for } \bar{x} \in [-0.005, 0.01]. \end{array}\right\} \quad (3.12)$$

According to the previous process of calculations, the initial configuration needs to be given first. For the vertical displacement, the initial conditions include six

Initial conditions	r_l (mm)	r_r (mm)	φ_l (deg.)	φ_r (deg.)	f_{net}^v (N m^{-1})	M (N)
Vertical	$(-2.753, 0.8344)$	$(3.451, 1.191)$	-47.72	-55.39	-0.4295	/
Rotational	$(-4.661, -0.4257)$	$(6.896, 0.2809)$	-20.99	-35.94	5.781×10^{-6}	3.033×10^{-5}

TABLE 2. Initial conditions in the models of vertical and rotational displacements. The density of the selected cross-section is given by $\rho_s = 0.5\rho$. The contact angle is given by $\theta = 2\pi/3$.

basic geometric quantities, which can be obtained by solving (2.2), (2.3) and (2.4a,b) with (3.12). Then the vertical resultant force can be calculated. For the rotational displacement, the initial conditions include not only the basic geometric quantities, but also the quantities that cannot be determined by the basic geometric quantities: the buoyancy, the weight force and their position vectors. It should be noted that the force balance conditions must be fulfilled for this initial configuration. For the configurations of force balance that are not easy to determine, the numerical results that are obtained by using the model of vertical displacement can be used as the initial conditions. The basic geometric quantities, the resultant forces and the resultant moments for the initial configurations are listed in table 2.

Referring to figure 8, this cross-section contains two sharp edges, so that the radii of curvature should be determined by a method analogous to that for the rectangles. For example, when the right contact point crosses the edge C, R_r can be given by

$$\left. \begin{array}{l} R_r = (1 + 40000\bar{x}_r^2)^{1.5}/200, \quad \text{for } \bar{\varphi}_r \leqslant \bar{\varphi}_r^*, \\ R_r = 0, \quad \text{for } \bar{\varphi}_r^* < \bar{\varphi}_r < \bar{\varphi}_r^* + \pi - \alpha_2, \\ R_r = \infty, \quad \text{for } \bar{\varphi}_r = \bar{\varphi}_r^* + \pi - \alpha_2, \end{array} \right\} \tag{3.13}$$

where $\bar{\varphi}_r^* = -\arctan 0.5$ and $\alpha_2 = \pi/4$. When the right contact point is on the interior of curve, R_r can also be easily determined by t_r. The case on the left side is the same as that on the right side.

In figure 9(a), the force profile and its first derivative are presented. The progress can be divided into four stages, which are clearly shown by the discontinuities of the first derivative $\dot{f}$. Referring to (2.14), the derivative $\dot{f}$ is determined by the basic geometric quantities and the radii of curvature, and the position vectors are continuous. Thus the jump or drop of $\dot{f}$ between two stages is closely related to the sudden change of the radius of the curvature. The vertical equilibrium is used as the initial conditions for the rotation (see table 2). The rotation process is more complex. The moment M and its derivative $\dot{M}$ are divided into eleven stages, as shown in figure 9(b). Because the rotation is periodic with period 2π, there are only ten stages for this rotation. The transition between two stages occurs when the contact point crosses the point (A, B or C). The points A and C are sharp edges, leading to two discontinuities of the radius of curvature, while only one discontinuity of the radius of curvature occurs at the point B. The rotational equilibria are also presented. The equilibria A and C are stable, and the equilibria B and D are unstable, where their stabilities are inferred from their derivatives $\dot{M}$. For the vertical and rotational displacements, the transitions between different stages can be viewed in supplementary movies 1 and 2, respectively (available at https://doi.org/10.1017/jfm.2018.323).
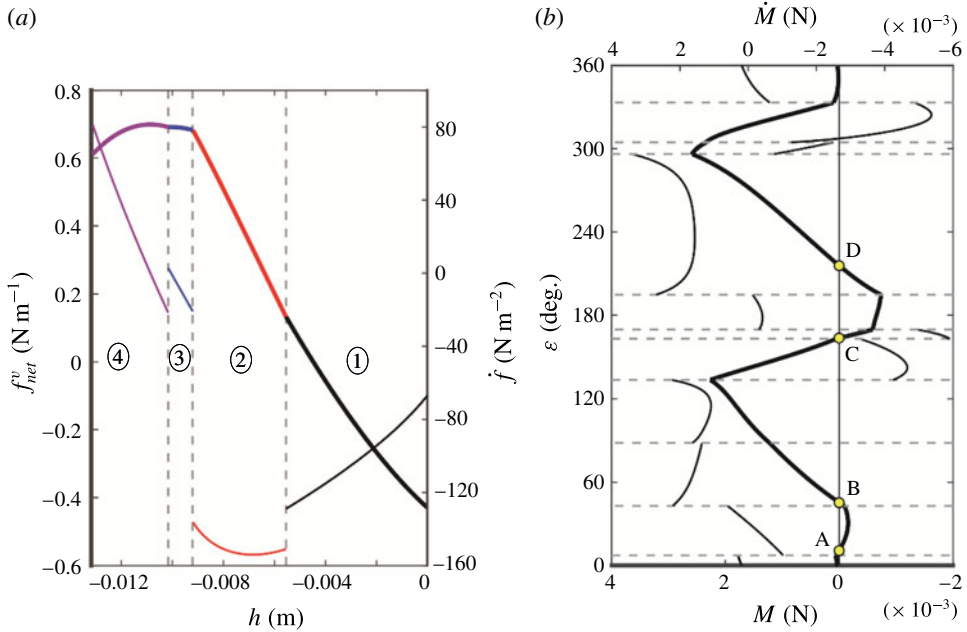
FIGURE 9. (Colour online) (*a*) The profiles of the resultant force and its derivative for the vertical displacement, and (*b*) the profiles of the resultant moment and its derivative for the rotational displacement. The thick lines in (*a*) and (*b*) denote the force and the moment, respectively, and the thin lines denote their derivatives. There are four equilibria in (*b*): $\varepsilon = 10.97°$ for A, $\varepsilon = 45.43°$ for B, $\varepsilon = 163.95°$ for C and $\varepsilon = 215.73°$ for D.

3.2. *Surface tension effects*

In this section, the surface tension effects on the vertical and rotational stabilities are investigated by using our model. As mentioned in previous sections, the configuration can be expressed by several quantities. Thus the surface tension effects can be studied by changing the quantities involved in the stability.

For the vertical displacement, the stabilities can be inferred from the derivative $\dot{f}$: $\dot{f} > 0$ corresponds to an unstable equilibrium while $\dot{f} < 0$ corresponds to a stable equilibrium. By substituting equations (2.2), (2.15*a–d*) and (2.16) into (2.14), the derivative $\dot{f} = \delta f_{net}^v / \delta h$ is given by

$$
\dot{f} = -\rho g D - \sigma \sqrt{\kappa} \left\{ \frac{\sqrt{\kappa} R_l \cos \phi_l \sin \varphi_l + \sin \left(\dfrac{\phi_l}{2} + \dfrac{\pi}{4} \right) \sin \phi_l}{\left[\sqrt{\kappa} R_l \cos \varphi_l + \sin \left(\dfrac{\phi_l}{2} + \dfrac{\pi}{4} \right) \right] \sin \left(\dfrac{\phi_l}{2} + \dfrac{\pi}{4} \right)} \right.
$$
$$
\left. + \frac{\sqrt{\kappa} R_r \cos \phi_r \sin \varphi_r + \sin \left(\dfrac{\phi_r}{2} + \dfrac{\pi}{4} \right) \sin \phi_r}{\left[\sqrt{\kappa} R_r \cos \varphi_r + \sin \left(\dfrac{\phi_r}{2} + \dfrac{\pi}{4} \right) \right] \sin \left(\dfrac{\phi_r}{2} + \dfrac{\pi}{4} \right)} \right\}, \tag{3.14}
$$

where $D = x_r - x_l$ denotes the horizontal distance between two contact points. Because there are too many variables involved in $\dot{f}$, only several representative quantities are
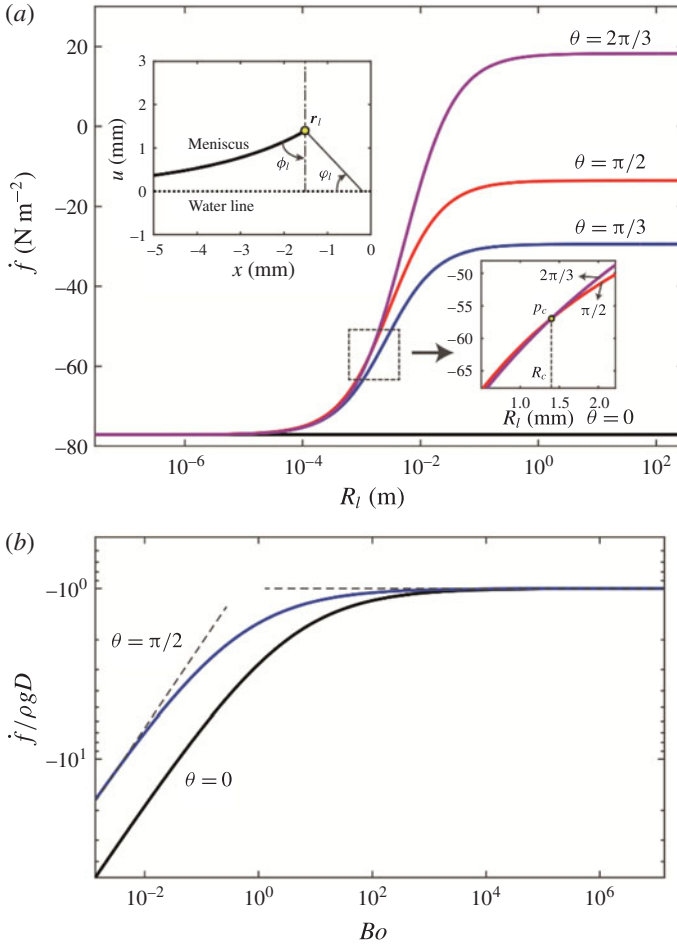
FIGURE 10. (Colour online) Surface tension effects on the vertical stability: (*a*) the effect of the radii of curvature and (*b*) the effect of the Bond number. The left inset in (*a*) shows the left part of the symmetric configuration of the case (i) $\phi_l = \pi/3$ and $x_l = -1.5$ mm for (*a*), while the configuration for (*b*) corresponds to the case (ii) $\phi_l = \pi/3$ and $R_l = R_r = 3$ mm. Because the floating body is convex, $\theta \in [0, \phi_l + \pi/2]$ for $\phi_l \in [0, \pi/2]$ and $\theta \in [\phi_l - \pi/2, \pi]$ for $\phi_l \in (\pi/2, \pi]$.

studied, including the distance D, the radii of curvature R_l and R_r. It is noted that the first term on the right-hand side of (3.14) is the same as the expression $\dot{f}$ for the case without surface tension. Then the surface tension effects on the vertical stability refer to the second term on the right-hand side of (3.14). In the second term, the effects at two contact points are independent and identical to each other, so that only the left side is taken into account.

Figure 10(*a*) shows the derivative $\dot{f}$ varying with the radii of curvature for the symmetric configurations (i.e. the right side is the mirror image of the left side with respect to $x = 0$) for different contact angles, where ϕ_l and x_l remain constant to keep the configuration unchanged (see the left inset). The additional diagrams for the mirror case of the origin configuration with respect to water line can be obtained by substituting θ with $\pi - \theta$ in figure 10(*a*). Assume without loss of generality that

$\phi_l \in [0, \pi/2]$. It is found that the smaller the radius of curvature, the better the stability of the floating body for $\theta \neq 0$. For $\theta = 0$, equation (3.14) can be reduced to

$$\dot{f} = -\rho g D - \sigma \sqrt{\kappa} \left[\frac{\sin \varphi_l}{\sin(\varphi_l/2 + \pi/4)} + \frac{\sin \varphi_r}{\sin(\varphi_r/2 + \pi/4)} \right], \qquad (3.15)$$

and therefore the radius of curvature has no effect on the vertical stability of the floating body. For $\theta \in [0, \pi/2]$, the vertical stability of floating body becomes better with the decrease of θ. For $\theta \in [\pi/2, \phi_l + \pi/2]$, the vertical stability of floating body with $R_l \geqslant R_c$ (see the critical point p_c in the right inset) becomes better with the decrease of θ, while the opposite is true for the floating body with $R_l < R_c$. It is also found that from $R_l \sim 10^{-4}$ to 10^{-1} there is a dramatic change in the vertical stability, implying that $R_l > 10^{-1}$ and $R_l < 10^{-4}$ have pretty much the same effects of $R_l = \infty$ and $R_l = 0$, respectively.

In figure 10(b), the relation between the dimensionless parameters $\dot{f}/\rho g D$ and the Bond number $Bo = \rho g D^2/\sigma$ is presented. For macroscale bodies ($Bo \gg 1$), the influence of surface tension is covered by the influence of gravity (see the horizontal dashed line). For microscale bodies ($Bo \to 0$), only the effects of surface tension exist (see the inclined dashed line). For mesoscale bodies ($Bo \sim 1$), the values of $\dot{f}$ vary continuously between the above two states, which may lead to the change of stability.

For the rotational displacement, a specific equilibrium configuration of the rectangle (see the inset in figure 11a) is considered to study the effects of surface tension on the rotational stability. It is well known that for a floating body without the surface tension effects the metacentric height ($\overline{GM}$) is a measurement of its rotational stability (Biran 2003). For a floating body under the surface tension effects, the derivative $\dot{M}$ can be used to determine the rotational stability. However, the expression of $\dot{M}$ is too complex to write here.

Figure 11(a) shows the derivative $\dot{M}$ varying with the radius of curvature R_l for the specific equilibrium configuration (see the inset), where $R_l = R_r$. The radii of curvature R_l and R_r at the contact points are varied artificially. Analogous to the vertical stability, the rotational stability will become better for smaller radii of curvature. Results show that in the range $R_l \sim 10^{-4}$ to 10^{-1} there is a dramatic change in the rotational stability, which is similar to the result of vertical stability, lead to a change in the rotational stability. Figure 11(b) shows the effect of size on the rotational stability. For comparison with the case without surface tension, the dimensionless parameter $\dot{M}/\rho g D^2 \overline{GM}$ is selected as the ordinate, because $\dot{M} = -\rho g D^2 \overline{GM}$ for the case without surface tension. The metacentric height is given by

$$\overline{GM} = \frac{5D}{96}, \qquad (3.16)$$

where $D = 2a$ is the characteristic length for the Bond number $Bo = \rho g D^2/\sigma$. It is found that when the Bond number is greater than 1000, the system tends towards the case without the surface tension effects. When the Bond number is less than 1, the gravity has no effect on the system.

4. Conclusions

In this paper, a model for calculating the force profile and the moment profile of a cylinder with an arbitrary cross-section is presented. The model first connects the basic geometric quantities and their derivatives to the configuration in which the menisci satisfy the Young–Laplace equation with Young's relation, and then transforms a number of irrelevant and repetitive problems of solving the resultant
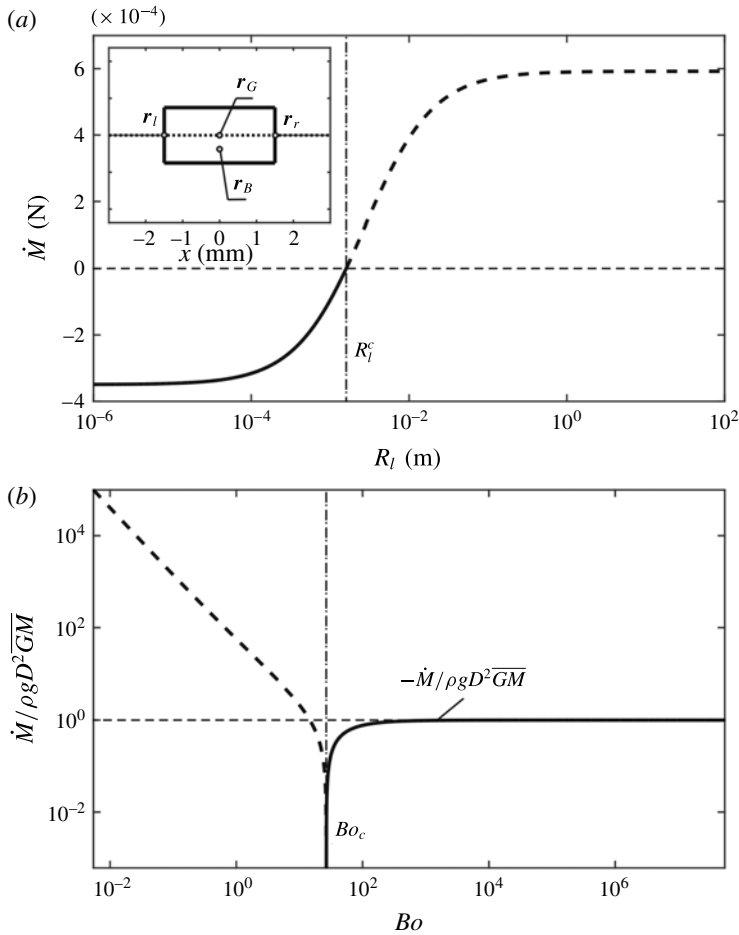
FIGURE 11. Surface tension effects on the rotational stability: (*a*) the effect of the radii of curvature and (*b*) the effect of the Bond number. The inset in (*a*) shows the configuration of the case (i) $\rho_s = 0.5\rho$, $\theta = \pi/2$, $\lambda = 0.5$ and $a = 1.5$ mm for (*a*), while the configuration for (*b*) corresponds to the case (ii) $\rho_s = 0.5\rho$, $\theta = \pi/2$, $\lambda = 0.5$ and $R_l = R_r = \infty$. The thick dashed lines denote the unstable equilibria while the thick solid lines correspond to the stable equilibria, where the thin vertical dot-dash lines correspond to the critical values $R_l^c = 1.598$ mm and $Bo_c = 26.59$, respectively. The horizontal dashed line in (*a*) represents the critical value of $\dot{M}$ and the horizontal dashed line in (*b*) corresponds to the case without the surface tension effects.

force and moment into a series of IVPs. Thus, the complex configurations can be obtained by integrating a simple case. Three different cross-sections are calculated by using the model to determine the vertical and rotational equilibria and their stabilities. Results show that the model can be applied to the convex floating bodies with finitely many sharp edges. In addition, there are some striking phenomena. For instance, the number of equilibria and their stabilities will change with the change of parameters for the cross-section of rectangle, indicating the bifurcation of the system.

The study is then extended to investigate the surface tension effects on the vertical and rotational stabilities in two dimensions by varying the parameters: the radii of

curvature and the size of the floating body. For the radii of curvature, in general the smaller the radii of curvature the better the vertical and rotational stabilities. However, for $\theta = 0$ (or $\theta = \pi$) the radii of curvature have no effect on the vertical stability of the floating body, referring to (3.15). Results also show in the range $R_l \sim 10^{-4}$ to 10^{-1} there is a dramatic change in the vertical and rotational stabilities, implying that $R_l > 10^{-1}$ and $R_l < 10^{-4}$ have pretty much the same effects as $R_l = \infty$ and $R_l = 0$, respectively. For macroscale bodies ($Bo \gg 1$), the influence of surface tension is covered by the influence of gravity. For microscale bodies ($Bo \to 0$), only the effects of surface tension exist. For mesoscale bodies ($Bo \sim 1$), the values of $\dot{f}$ and $\dot{M}$ vary continuously between the above two states, which may lead to the change of stability.

Acknowledgement

Supplementary movies

Supplementary movies are available at https://doi.org/10.1017/jfm.2018.323.

Appendix A.

Finn (1988) found that an axisymmetric meniscus can be uniquely determined by the contact angle and volume in an axisymmetric container convex to the liquid. Following Finn (1988), we consider a convex cylinder floating on the surface of a liquid with a given contact angle and a given position and orientation. For simplicity, only the configuration on the left side is considered (see figure 1c). The cylinder surface on the left side can be expressed by the single-valued function $x = x(y)$, which is convex leftward. Thus the $x'(y) = \mathrm{d}x/\mathrm{d}y$ derivative is monotonically non-decreasing on that interval. Substituting (2.4a) into $x'(y) = \mathrm{d}x/\mathrm{d}y$, it is easy to find that $\varphi_l(y)$ is also monotonically non-decreasing. Substituting (2.4b) into (2.2) and then using the geometric relation (2.3), the meniscus can be found as the solution of equation

$$\psi_l(y) + \varphi_l(y) + \theta - \pi/2 = 0, \tag{A 1}$$

where $\psi_l(y)$ is strictly increasing. We assume the existence of the solution of (A 1). Then the solution of (A 1) is uniquely determined, because the function $\psi_l(y) + \varphi_l(y)$ is strictly increasing. It is noted the condition that the cylinder is convex is sufficient but not necessary for the uniqueness of the meniscus, similar to the condition for the uniqueness of the meniscus in an axisymmetric container presented by Finn (1988).

Appendix B.

An infinitesimal displacement in h will result in the displacements: δr_l, δr_r, $\delta \varphi_l$ and $\delta \varphi_r$, as shown in figure 2(a). For simplicity, only the case on the left side is considered. From equations (2.2), (2.3) and (2.4a,b), the variations $\delta \varphi_l$, δt_l, δu_l and δh are related by

$$\delta u_l = -\frac{1}{\sqrt{\kappa}} \sin\left(\frac{\varphi_l + \theta}{2} + \frac{\pi}{4} \right) \delta \varphi_l, \tag{B 1}$$

$$\left. \frac{x''y' - x'y''}{y'^2} \right|_{t=t_l} \delta t_l = \frac{1}{\cos^2 \varphi_l} \delta \varphi_l, \tag{B 2}$$

$$y'(t_l)\delta t_l + \delta h = \delta u_l, \tag{B 3}$$

so that

$$\delta u_l = -\frac{1}{\sqrt{\kappa}} \sin\left(\frac{\varphi_l + \theta}{2} + \frac{\pi}{4}\right) \left.\frac{x''y' - x'y''}{y'^3}\right|_{t=t_l} \cos^2 \varphi_l (\delta u_l - \delta h). \tag{B 4}$$

Because the parametrization of the cylinder is oriented counterclockwise, the signed curvature k at the left contact point is shown as

$$k \equiv \frac{1}{R_l} = \left.\frac{x'y'' - x''y'}{(x'^2 + y'^2)^{3/2}}\right|_{t=t_l}. \tag{B 5}$$

From the geometric relation at the left contact point, we have

$$\cos \varphi_l = -\left.\frac{y'}{\sqrt{x'^2 + y'^2}}\right|_{t=t_l}. \tag{B 6}$$

By substituting equations (B 5) and (B 6) into (B 4), we obtain

$$\delta u_l = \frac{\sin\left(\dfrac{\varphi_l + \theta}{2} + \dfrac{\pi}{4}\right)}{\sqrt{\kappa} R_l \cos \varphi_l + \sin\left(\dfrac{\varphi_l + \theta}{2} + \dfrac{\pi}{4}\right)} \delta h. \tag{B 7}$$

From equations (B 1) and (B 7), the variation $\delta\varphi_l$ can also be determined. When the cylinder is considered as the reference frame (see figure 2b), the variation $\delta\bar{r}_l$ is given by

$$\delta\bar{r}_l = (\delta x_l, \delta u_l - \delta h), \tag{B 8}$$

so that δx_l and δu_l satisfy the relation

$$\tan \varphi_l (\delta u_l - \delta h) = \delta x_l. \tag{B 9}$$

Thus the variation δx_l is obtained. The derivations for the variations δr_r and $\delta\varphi_r$ at the right contact point are similar to those at the left contact point.

For the variation δV_B, the derivation is based on the selection of the cylinder used as the reference frame. The variation δV_B to the first order in δh is the area of the quadrilateral, where the position vectors of four vertices of the quadrilateral are r_l, r_r, $r_r + \delta\bar{r}_r$ and $r_l + \delta\bar{r}_l$:

$$\delta V_B = \frac{1}{2}|AC \times BD|, \tag{B 10}$$

where the quadrilateral $ABCD$ is oriented counterclockwise, so that the vectors AC and BD are given by

$$\left.\begin{aligned} AC &= \delta\bar{r}_r + r_r - r_l, \\ BD &= \delta\bar{r}_l + r_l - r_r. \end{aligned}\right\} \tag{B 11}$$

By substituting (B 11) into (B 10), δV_B can be expressed in terms of the vectors of the contact points and their variations:

$$\delta V_B = \frac{1}{2}[(u_l - u_r)(\delta x_r + \delta x_l) + (x_r - x_l)(\delta u_l + \delta u_r - 2\delta h)]. \tag{B 12}$$

Appendix C.

An infinitesimal rotational displacement $\delta\varepsilon$ of the cylinder will result in the displacements: δr_l, δr_r, $\delta\varphi_l$ and $\delta\varphi_r$, as shown in figure 4(a). For simplicity, only the case on the left side is considered. Similar to the derivations in appendix B, the

variations $\delta\varphi_l$ and δu_l still satisfy the relation (B 1). For the rotation, equation (B 2) is modified to

$$\left.\frac{\tilde{x}''\tilde{y}' - \tilde{x}'\tilde{y}''}{\tilde{y}'^2}\right|_{t=t_l} \delta t = \frac{1}{\cos^2\tilde{\varphi}_l}\delta\tilde{\varphi}_l, \tag{C 1}$$

which is established on the surface of the cylinder after rotation (designated by the tildes over characters). Referring to figure 12, the geometric relation gives

$$-\delta\varphi_l = -\delta\tilde{\varphi}_l + \delta\varepsilon. \tag{C 2}$$

For the infinitesimal rotation, the tildes in the non-infinitesimal quantities in (C 1) can be removed. Substituting (C 2) into (C 1), we obtain

$$\left.\frac{x''y' - x'y''}{y'^2}\right|_{t=t_l} \delta t = \frac{1}{\cos^2\varphi_l}(\delta\varphi_l + \delta\varepsilon). \tag{C 3}$$

For the rotation, equation (B 3) is modified to

$$y'(t_l)\delta t + (x_l - x_{ro})\delta\varepsilon = \delta u_l. \tag{C 4}$$

Substituting equations (B 5), (B 6), (C 3) and (C 4) into (B 1), we obtain

$$\delta u_l = \frac{\sin\left(\dfrac{\varphi_l+\theta}{2} + \dfrac{\pi}{4}\right)\cos\varphi_l(R_l - L_l)}{\sqrt{\kappa}\cos\varphi_l R_l + \sin\left(\dfrac{\varphi_l+\theta}{2} + \dfrac{\pi}{4}\right)}\delta\varepsilon. \tag{C 5}$$

From equations (B 1) and (C 5), the variation $\delta\varphi_l$ can also be determined. Considering the cylinder after rotation as a reference frame (see figure 12), the variation $\delta\tilde{\boldsymbol{r}}_l$ is given by

$$\delta\tilde{\boldsymbol{r}}_l = [\delta x_l + (u_l - u_{ro})\delta\varepsilon,\ \delta u_l - (x_l - x_{ro})\delta\varepsilon], \tag{C 6}$$

so that δx_l and δu_l satisfy the relation

$$\tan\varphi_l[\delta u_l - (x_l - x_{ro})\delta\varepsilon] = \delta x_l + (u_l - u_{ro})\delta\varepsilon. \tag{C 7}$$

Thus the variation δx_l is obtained. The derivations for the variations $\delta\boldsymbol{r}_r$ and $\delta\varphi_r$ at the right contact point are similar to those at the left contact point.

In the context of rotation, the change of V_B to the first order in $\delta\varepsilon$, i.e. the quadrilateral *ABCD* for the variation δV_B (see figure 12*b*), is obtained by replacing the tildes with the bars over the characters in (B 10) and (B 11). The variations $\delta\bar{\boldsymbol{r}}_l$ and $\delta\bar{\boldsymbol{r}}_r$ are obtained based on the cylinder before rotation chosen as the reference frame, while the variations $\delta\tilde{\boldsymbol{r}}_l$ and $\delta\tilde{\boldsymbol{r}}_r$ correspond to the cylinder after rotation chosen as the reference frame. The relation of these variations can be described as

$$[\delta\bar{\boldsymbol{r}}_l^T, \delta\bar{\boldsymbol{r}}_r^T] = \begin{bmatrix}\cos\varepsilon & \sin\varepsilon\\ -\sin\varepsilon & \cos\varepsilon\end{bmatrix}[\delta\tilde{\boldsymbol{r}}_l^T, \delta\tilde{\boldsymbol{r}}_r^T]. \tag{C 8}$$

The variation δM_t can be obtained by substituting

$$\left.\begin{aligned}\delta\boldsymbol{f}_t^l &= -\sigma\cos(\varphi_l+\theta)\delta\varphi_l\boldsymbol{e}_i + \sigma\sin(\varphi_l+\theta)\delta\varphi_l\boldsymbol{e}_j,\\ \delta\boldsymbol{f}_t^r &= \sigma\cos(\varphi_r+\theta)\delta\varphi_r\boldsymbol{e}_i + \sigma\sin(\varphi_r+\theta)\delta\varphi_r\boldsymbol{e}_j\end{aligned}\right\} \tag{C 9}$$

into (2.23*a*). Equation (C 9) is derived from equations (2.7*a,b*).
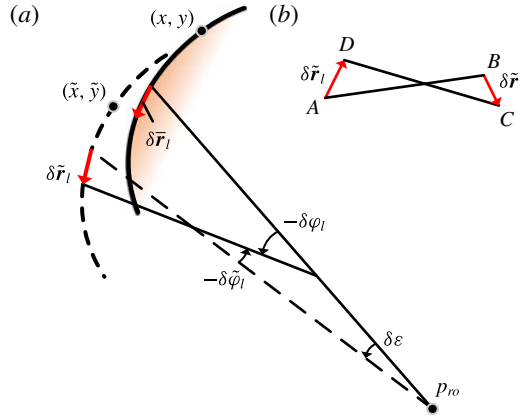
FIGURE 12. (Colour online) (*a*) The geometric relation between configurations before and after an infinitesimal rotation and (*b*) the quadrilateral *ABCD* for determining the variations δr_B and δV_B.

The moment M_p can be expressed as follows:

$$M_p \equiv |\mathbf{r}_p \times \mathbf{f}_p| = \frac{\rho g}{6} \left[x_l^2 (2u_l + u_r) - x_r^2 (2u_r + u_l) \right.$$
$$\left. + x_l x_r (u_r - u_l) + 2u_l^3 - 2u_r^3 \right], \tag{C 10}$$

where $\mathbf{r}_p$ and $\mathbf{f}_p$ are given by (2.30) and (2.10), respectively. Then, the variation δM_p can be obtained by calculating the variation of (C 10) and neglecting the higher-order terms $o(\delta \varepsilon)$. Then (2.29*b*) is derived.

For the variation δM_B, the variation $\delta \mathbf{B}$ in (2.23*c*) is given by

$$\delta \mathbf{B} = \rho g \delta V_B \mathbf{e}_j. \tag{C 11}$$

The centroid of the buoyancy $\mathbf{r}_B$ is given by

$$\mathbf{r}_B = \frac{S_y}{V_B} \mathbf{e}_i + \frac{S_x}{V_B} \mathbf{e}_j. \tag{C 12}$$

Thus, from (C 12) the variation $\delta \tilde{\mathbf{r}}_B$ is obtained as

$$\delta \tilde{\mathbf{r}}_B = \frac{\delta S_y - x_B \delta V_B}{V_B} \mathbf{e}_i + \frac{\delta S_x - u_B \delta V_B}{V_B} \mathbf{e}_j, \tag{C 13}$$

where δS_y and δS_x are the first moments of area of the quadrilateral *ABCD* in the y and x directions, respectively. They can be given by

$$\left. \begin{aligned} 6\delta S_y &= \sum_{i=0}^{3} (x_i + x_{i+1})(x_i u_{i+1} + x_{i+1} u_i), \\ 6\delta S_x &= \sum_{i=0}^{3} (u_i + u_{i+1})(x_i u_{i+1} + x_{i+1} u_i), \end{aligned} \right\} \tag{C 14}$$

where the subscripts i denote the vertices: $0, 4 \rightarrow A$, $1 \rightarrow B$, $2 \rightarrow C$ and $3 \rightarrow D$. Neglecting the higher-order terms, δS_y and δS_x can be expressed in terms of the first order in $\delta\varepsilon$. Considering the water line as the reference frame, $\delta\boldsymbol{r}_B$ and $\delta\tilde{\boldsymbol{r}}_B$ satisfy the relation:

$$\left.\begin{array}{l} \delta x_B - \delta\tilde{x}_B = -(u_B - u_{ro})\delta\varepsilon, \\ \delta u_B - \delta\tilde{u}_B = (x_B - x_{ro})\delta\varepsilon. \end{array}\right\} \tag{C 15}$$

Substituting (C 11), (C 13) and (C 15) into (2.23c), the variation δM_B is obtained.

The variation δM_G can be easily derived by substituting (2.31) into (2.23d). Finally the variation δM is derived.

REFERENCES

ASPLEY, A., HE, C. & McCUAN, J. 2015 Force profiles for parallel plates partially immersed in a liquid bath. *J. Math. Fluid Mech.* **17**, 87–102.

BHATNAGAR, R. & FINN, R. 2006 Equilibrium configurations of an infinite cylinder in an unbounded fluid. *Phys. Fluids* **18**, 047103.

BHATNAGAR, R. & FINN, R. 2016 On the capillarity equation in two dimensions. *J. Math. Fluid Mech.* **18**, 731–738.

BIRAN, A. 2003 Basic ship hydrostatics. In *Ship Hydrostatics and Stability*, pp. 23–70. Butterworth–Heinemann.

BOWDEN, N., TERFORT, A., CARBECK, J. & WHITESIDES, G. M. 1997 Self-assembly of mesoscale objects into ordered two-dimensional arrays. *Science* **276**, 233–235.

BRAKKE, K. A. 1992 The surface evolver. *Exp. Math.* **1**, 141–165.

CHAN, D. Y. C., HENRY, J. D. & WHITE, L. R. 1981 The interaction of colloidal particles collected at fluid interfaces. *J. Colloid Interface Sci.* **79**, 410–418.

CHEN, H. & SIEGEL, D. J. 2018 A floating cylinder on an unbounded bath. *J. Math. Fluid Mech.*; doi:10.1007/s00021-018-0372-7 In press. First Online: 28 March 2018.

CONCUS, P. 1968 Static menisci in a vertical right circular cylinder. *J. Fluid Mech.* **34**, 481–495.

FINN, R. 1988 Non uniqueness and uniqueness of capillary surfaces. *Manuscr. Math.* **61**, 347–372.

FINN, R. 2010 On Young's paradox, and the attractions of immersed parallel plates. *Phys. Fluids* **22**, 017103.

HUH, C. & MASON, S. G. 1974 The flotation of axisymmetric particles at horizontal liquid interfaces. *J. Colloid Interface Sci.* **47**, 271–289.

JANSSENS, S., CHAURASIA, V. & FRIED, E. 2017 Effect of a surface tension imbalance on a partly submerged cylinder. *J. Fluid Mech.* **830**, 369–386.

KELLER, J. B. 1998 Surface tension force on a partly submerged body. *Phys. Fluids* **10**, 3009–3010.

KEMP, T. M. & SIEGEL, D. 2011 Floating bodies in two dimensions without gravity. *Phys. Fluids* **23**, 043303.

KRALCHEVSKY, P. A., PAUNOV, V. N., IVANOV, I. B. & NAGAYAMA, K. 1992 Capillary meniscus interaction between colloidal particles attached to a liquid – fluid interface. *J. Colloid Interface Sci.* **151**, 79–94.

LIU, J. L., FENG, X. Q. & WANG, G. F. 2007 Buoyant force and sinking conditions of a hydrophobic thin rod floating on water. *Phys. Rev.* E **76**, 066103.

MAJUMDAR, S. R. & MICHAEL, D. H. 1976 The equilibrium and stability of two dimensional pendent drops. *Proc. R. Soc. Lond.* A **351**, 89–115.

MANSFIELD, E. H., SEPANGI, H. R. & EASTWOOD, E. A. 1997 Equilibrium and mutual attraction or repulsion of objects supported by surface tension. *Phil. Trans. R. Soc. Lond.* A **355**, 869–919.

MIERSEMANN, E. 2015 Lecture Notes, 'Liquid Interfaces', Version November 2015, pp. 54–56. See http://www.math.uni-leipzig.de/~miersemann/.

NICOLSON, M. M. 1949 The interaction between floating particles. *Proc. Camb. Phil. Soc.* **45**, 288–295.

OETTEL, M., DOMINGUEZ, A. & DIETRICH, S. 2005 Effective capillary interaction of spherical particles at fluid interfaces. *Phys. Rev.* E **71**, 051401.

OLIVER, J. F., HUH, C. & MASON, S. G. 1977 Resistance to spreading of liquids by sharp edges. *J. Colloid Interface Sci.* **59**, 568–581.

PADDAY, J. F. 1971 The profiles of axially symmetric menisci. *Phil. Trans. R. Soc. Lond.* A **269**, 265–293.

PAUNOV, V. N., KRALCHEVSKY, P. A., DENKOV, N. D., IVANOV, I. B. & NAGAYAMA, K. 1992 Capillary meniscus interaction between a microparticle and a wall. *Colloid Surf.* **67**, 119–138.

PRINCEN, H. M. 1969 The equilibrium shape of interfaces, drops, and bubbles. Rigid and deformable particles at interfaces. In *Surface and Colloid Science* (ed. E. Matijević), vol. 2, pp. 1–84. Wiley.

RAPACCHIETTA, A. V., NEUMANN, A. W. & OMENYI, S. N. 1977 Force and free-energy analyses of small particles at fluid interfaces: I. Cylinders. *J. Colloid Interface Sci.* **59**, 541–554.

RAPHAËL, E., DI MEGLIO, J. M., BERGER, M. & CALABI, E. 1992 Convex particles at interfaces. *J. Phys.* I **2**, 571–579.

SINGH, P. & HESLA, T. I. 2004 The interfacial torque on a partially submerged sphere. *J. Colloid Interface Sci.* **280**, 542–543.

SOLIGNO, G., DIJKSTRA, M. & VAN ROIJ, R. 2014 The equilibrium shape of fluid–fluid interfaces: Derivation and a new numerical method for Young's and Young–Laplace equations. *J. Chem. Phys.* **141**, 244702.

SOLIGNO, G., DIJKSTRA, M. & VAN ROIJ, R. 2016 Self-assembly of cubes into 2D hexagonal and honeycomb lattices by hexapolar capillary interactions. *Phys. Rev. Lett.* **116**, 258001.

STAMOU, D., DUSCHL, C. & JOHANNSMANN, D. 2000 Long-range attraction between colloidal spheres at the air–water interface: The consequence of an irregular meniscus. *Phys. Rev.* E **62**, 5263–5272.

TAVACOLI, J. W., KATGERT, G., KIM, E. G., CATES, M. E. & CLEGG, P. S. 2012 Size limit for particle-stabilized emulsion droplets under gravity. *Phys. Rev. Lett.* **108**, 268306.

TREINEN, R. 2016 Examples of non-uniqueness of the equilibrium states for a floating Ball. *Adv. Mater. Phys. Chem.* **6**, 177–194.

VELLA, D. 2015 Floating versus sinking. *Annu. Rev. Fluid Mech.* **47**, 115–135.

VELLA, D., LEE, D. G. & KIM, H. Y. 2006 The load supported by small floating objects. *Langmuir* **22**, 5979–5981.

ZHOU, X. & ZHANG, F. 2017 Bifurcation of a partially immersed plate between two parallel plates. *J. Fluid Mech.* **817**, 122–137.